Monthly Notices
of the
ROYAL ASTRONOMICAL SOCIETY

Mon. Not. R. Astron. Soc. **419,** 2545–2578 (2012) doi:10.1111/j.1365-2966.2011.19905.x

Herschel⋆-ATLAS/GAMA: dusty early-type galaxies and passive spirals

K. Rowlands,[1]† L. Dunne,[1] S. Maddox,[1] N. Bourne,[1] H. L. Gomez,[2] S. Kaviraj,[3] S. P. Bamford,[1] S. Brough,[4] S. Charlot,[5] E. da Cunha,[6] S. P. Driver,[7,8] S. A. Eales,[2] A. M. Hopkins,[4] L. Kelvin,[7,8] R. C. Nichol,[9] A. E. Sansom,[10] R. Sharp,[11] D. J. B. Smith,[1,12] P. Temi,[13] P. van der Werf,[14] M. Baes,[15] A. Cava,[16] A. Cooray,[17] S. M. Croom,[18] A. Dariush,[3] G. De Zotti,[19,20] S. Dye,[1,2] J. Fritz,[15] R. Hopwood,[3] E. Ibar,[21] R. J. Ivison,[21,22] J. Liske,[23] J. Loveday,[24] B. Madore,[25] P. Norberg,[22] C. C. Popescu,[10] E. E. Rigby,[1,22] A. Robotham,[7] G. Rodighiero,[19] M. Seibert[25] and R. J. Tuffs[26]

[1]*School of Physics & Astronomy, The University of Nottingham, University Park Campus, Nottingham NG7 2RD*
[2]*School of Physics & Astronomy, Cardiff University, Queens Buildings, The Parade, Cardiff CF24 3AA*
[3]*Department of Physics, Imperial College London, Prince Consort Road, London SW7 2AZ*
[4]*Australian Astronomical Observatory, PO Box 296, Epping, NSW 1710, Australia*
[5]*Institut d'Astrophysique de Paris, CNRS, Université Pierre & Marie Curie, UMR 7095, 98bis bd Arago, 75014 Paris, France*
[6]*Max Planck Institute for Astronomy, Konigstuhl 17, 69117 Heidelberg, Germany*
[7]*International Centre for Radio Astronomy (ICRAR), University of Western Australia, Crawley, WA 6009, Australia*
[8]*(SUPA) School of Physics & Astronomy, University of St Andrews, North Haugh, St Andrews KY16 9SS*
[9]*Institute of Cosmology and Gravitation (ICG), Dennis Sciama Building, Burnaby Road, Portsmouth PO1 3FX*
[10]*Jeremiah Horrocks Institute, University of Central Lancashire, Preston PR1 2HE*
[11]*Research School of Astronomy & Astrophysics, Mount Stromlo Observatory, Cotter Road, Weston Creek, ACT 2611, Australia*
[12]*Centre for Astrophysics, Science & Technology Research Institute, University of Hertfordshire, Hatfield, Herts AL10 9AB*
[13]*Astrophysics Branch, NASA Ames Research Center, Mail Stop 2456, Moffett Field, CA 94035, USA*
[14]*Leiden University, PO Box 9500, 2300 RA Leiden, the Netherlands*
[15]*Sterrenkundig Observatorium, Universiteit Gent, Krijgslaan 281 S9, B-9000 Gent, Belgium*
[16]*Departamento de Astrofísica, Facultad de CC. Físicas, Universidad Complutense de Madrid, E-28040 Madrid, Spain*
[17]*Department of Physics and Astronomy, University of California, Irvine, CA 92697, USA*
[18]*Sydney Institute for Astronomy, School of Physics, University of Sydney, NSW 2006, Australia*
[19]*INAF – University of Padova, Department of Astronomy, Vicolo Osservatorio 3, I-35122 Padova, Italy*
[20]*SISSA, Via Bonomea 265, I-34136 Trieste, Italy*
[21]*UK Astronomy Technology Centre, Royal Observatory, Edinburgh EH9 3HJ*
[22]*Institute for Astronomy, University of Edinburgh, Royal Observatory, Blackford Hill, Edinburgh EH9 3HJ*
[23]*European Southern Observatory, Karl-Schwarzschild-Str. 2, 85748 Garching, Germany*
[24]*Astronomy Centre, University of Sussex, Falmer, Brighton BN1 9QH*
[25]*Observatories of the Carnegie Institution of Washington, 813 Santa Barbera Street, Pasadena, CA 91101, USA*
[26]*Max Planck Institute for Nuclear Physics (MPIK), Saupfercheckweg 1, 69117 Heidelberg, Germany*

Accepted 2011 September 27. Received 2011 September 22; in original form 2011 July 19

ABSTRACT

We present the dust properties and star formation histories of local submillimetre-selected galaxies, classified by optical morphology. Most of the galaxies are late types and very few are early types. The early-type galaxies (ETGs) that are detected contain as much dust as typical spirals, and form a unique sample that has been blindly selected at submillimetre wavelengths. Additionally, we investigate the properties of the most passive, dusty spirals.

We morphologically classify 1087 galaxies detected in the *Herschel*-Astrophysical Terahertz Large Area Survey (H-ATLAS) Science Demonstration Phase data. Comparing to a control

⋆*Herschel* is an ESA space observatory with science instruments provided by European-led Principal Investigator consortia and with important participation from NASA.

†E-mail: ppxkr@nottingham.ac.uk

sample of optically selected galaxies, we find 5.5 per cent of luminous ETGs are detected in H-ATLAS. The H-ATLAS ETGs contain a significant mass of cold dust: the mean dust mass is $5.5 \times 10^7\,M_\odot$, with individual galaxies ranging from 9×10^5 to $4 \times 10^8\,M_\odot$. This is comparable to that of spiral galaxies in our sample, and is an order of magnitude more dust than that found for the control early-types, which have a median dust mass inferred from stacking of $(0.8–4.0) \times 10^6\,M_\odot$ for a cold dust temperature of 25–15 K. The early-types detected in H-ATLAS tend to have bluer $NUV - r$ colours, higher specific star formation rates and younger stellar populations than early-types which are optically selected, and may be transitioning from the blue cloud to the red sequence.

We also find that H-ATLAS and control early-types inhabit similar low-density environments. We investigate whether the observed dust in H-ATLAS early-types is from evolved stars, or has been acquired from external sources through interactions and mergers. We conclude that the dust in H-ATLAS and control ETGs cannot be solely from stellar sources, and a large contribution from dust formed in the interstellar medium or external sources is required. Alternatively, dust destruction may not be as efficient as predicted. We also explore the properties of the most passive spiral galaxies in our sample with specific star formation rate (SSFR) $< 10^{-11}\,yr^{-1}$. We find these passive spirals have lower dust-to-stellar mass ratios, higher stellar masses and older stellar population ages than normal spirals. The passive spirals inhabit low-density environments similar to those of the normal spiral galaxies in our sample. This shows that the processes which turn spirals passive do not occur solely in the intermediate-density environments of group and cluster outskirts.

Key words: dust, extinction – galaxies: elliptical and lenticular, cD – galaxies: evolution – infrared: galaxies – submillimetre: galaxies.

1 INTRODUCTION

It has long been known that there is a relationship between galaxy optical colour and morphology. Galaxies can be split into a red sequence and blue cloud (Tresse et al. 1999; Strateva et al. 2001; Blanton et al. 2003; Baldry et al. 2004; Bell et al. 2004). Red galaxies are generally passive early-type galaxies (ETGs; those that have elliptical or S0 morphology), but with ∼25 per cent being spirals which are red either due to dust or because they are passive (Driver et al. 2006). Blue galaxies are actively star forming and mostly of spiral or irregular morphology. The colour bimodality of galaxies is linked to their star formation history (SFH), with the stellar population of galaxies transitioning from blue to red as their star formation ceases due to the removal or consumption of cold gas (e.g. Faber et al. 2007; Hughes & Cortese 2009). The injection of gas and dust via mergers may temporarily rejuvenate star formation, and so this evolution of colour can be reversed (Cortese & Hughes 2009; Kannappan, Guie & Baker 2009; Wei et al. 2010). Such 'rejuvenators' may have had substantially different star formation histories from those which make up the majority of their morphological type, and may provide insight into the evolutionary processes that shape galaxies today.

Massive ($>10^{10}\,M_\odot$) ETGs are traditionally thought to be 'red and dead' (e.g. Temi, Brighenti & Mathews 2009b), having formed most of their stellar mass at early epochs over a relatively short period of time (e.g. Cimatti et al. 2004; Thomas et al. 2005) and then evolved passively to their present state. Their optical light is dominated by old stellar populations; however, recent ultra-violet (UV) studies of large samples of ETGs have shown that many of these galaxies exhibit low to moderate levels of star formation (Yi et al. 2005; Schawinski et al. 2007a; Kaviraj et al. 2007, 2008, 2011a; Kaviraj 2010). The UV-optical colours suggest that at least ∼30 per cent of UV-selected ETGs at $z < 0.11$ have evidence of recent star formation within the last 1 Gyr (Kaviraj et al. 2007); however, it is difficult to determine the contribution of UV flux from old stars.

Mergers are likely to trigger star formation, since a high incidence of ETGs with disturbed morphologies (18 per cent) has been observed (Kaviraj 2010), and these disturbed ETGs also have bluer $NUV - r$ colours than normal ETGs. The major merger rate at low and intermediate redshifts is thought to be too low to account for the number of galaxies which have disturbed morphologies (e.g. De Propris et al. 2007, 2010; Lotz et al. 2008), therefore Kaviraj et al. (2011a) conclude that minor mergers are the most likely trigger of recent star formation in ETGs.

Although there is evidence for limited quantities of dust in ETGs, these galaxies are generally thought to be gas- and dust-poor, which gives an insight into their evolutionary state. UV starlight is preferentially absorbed and re-emitted by dust in the far-infrared (FIR) and submillimetre, so the presence of dust emission is often viewed as evidence for ongoing star formation (Kennicutt 1998), although dust can also be heated by the radiation field of an old stellar population. Evidence for dust in ETGs was first found in the optical (e.g. Hawarden et al. 1981; Sadler & Gerhard 1985; van Dokkum & Franx 1995), yet it is difficult to estimate the total dust mass purely from optical observations. Warm dust (>30 K) was detected in 12 per cent of local ETGs by *IRAS* (Bregman et al. 1998), but *IRAS* was less sensitive to the cold dust component which dominates the dust mass in local galaxies (Dunne & Eales 2001; Vlahakis, Dunne & Eales 2005; Smith et al. 2011b). There have been few studies of ETGs at FIR-submillimetre wavelengths to date, since surveys conducted at these wavelengths have been limited in areal coverage. Consequently, studies of ETGs have been targeted observations of relatively small, and often biased, samples. Cold dust has been

detected in ETGs through observations with *ISO*, Submillimetre Common-User Bolometer Array (SCUBA), *Spitzer* and SHARC II (Temi et al. e.g. 2004; Leeuw et al. 2004, 2008; Vlahakis et al. 2005; Temi, Brighenti & Mathews 2007; Stickel, Klaas & Lemke 2007; Savoy, Welch & Fich 2009). Cold dust has also been observed by *Herschel* in 10 nearby ETGs (Skibba et al. 2011), and in the Virgo cluster elliptical galaxy M86, which contains dust stripped from the nearby spiral NGC 4438 (Cortese et al. 2010; Gomez et al. 2010).

Conversely, spiral galaxies are generally rich in dust and gas, and make up the majority of the star-forming population. Their blue optical colours indicate young stellar populations, yet for some time optically red spirals with no spectroscopic evidence of star formation have been known to exist in the outskirts of clusters (van den Bergh 1976; Poggianti et al. 1999, 2004; Goto et al. 2003). These spirals can be red due to dust obscuration, or because of an ageing stellar population (Wolf et al. 2009). It is generally believed that passive red spirals have had their star formation quenched due to environmental effects, since they are found to mostly reside in intermediate-density environments (Bamford et al. 2009; Skibba et al. 2009; Masters et al. 2010b). The star formation rate (SFR) was found to be lower for red spirals than blue spirals in all environments, which indicates that factors other than environment can truncate star formation in red spirals (Bamford et al. 2009; Masters et al. 2010b). The same authors also find that a large fraction of red spirals are massive ($>10^{10}\,M_{\odot}$).

We can now get an unprecedented view of dust in local galaxies from the *Herschel*-ATLAS survey (H-ATLAS; Eales et al. 2010). The telescope observes at FIR-submillimetre wavelengths across the peak of the dust emission, making it an unbiased tracer of the dust mass in galaxies. In this paper we examine the properties of galaxies detected in the H-ATLAS Science Demonstration Phase (SDP) field as a function of morphological type, and highlight interesting populations which do not conform to the usual trend of colour and morphology. In particular, we focus our analysis on the properties of H-ATLAS ETGs and how these galaxies are different from optically selected ETGs, in addition to studying a population of dusty, passive spirals. We present the detection of the dustiest ETGs in a large area blind submillimetre survey with *Herschel*, where the lack of pre-selection in other bands makes it the first unbiased survey for cold dust in ETGs. In Section 2 we describe the survey, observations and morphological classifications, and present the spectral energy distribution (SED) fitting method to explore the properties and SFHs of galaxies in our sample, the results of which are presented in Section 3. The properties of a population of passive spirals are examined in Section 4. The AGN fraction of dusty ETGs is explored in Section 5, and we investigate whether environment may be an influential factor in the properties of our galaxies in Section 6. The submillimetre detected ETGs are compared to a control sample of optically selected ETGs in Section 7; and we discuss the origin of the dust in Section 8. We adopt a cosmology with $\Omega_{\rm m} = 0.27$, $\Omega_{\Lambda} = 0.73$ and $H_0 = 71\,{\rm km\,s^{-1}\,Mpc^{-1}}$.

2 OBSERVATIONS AND SAMPLE SELECTION

The H-ATLAS (Eales et al. 2010) is a $\sim$570 deg^2 survey undertaken by the *Herschel Space Observatory* (Pilbratt et al. 2010) at 100, 160, 250, 350 and 500 μm to provide an unbiased view of the submillimetre Universe. Observations are carried out in parallel mode using the Photodetector Array Camera (PACS) (Poglitsch et al. 2010) and Spectral and Photometric Imaging Receiver (SPIRE) (Griffin et al. 2010) instruments simultaneously. In this paper, we use observations in the SDP field, with an area of $\sim$14 deg^2 centred on $\alpha = 09^{\rm h}05^{\rm m}30\overset{\rm s}{.}0$, $\delta = 00^{\circ}30'00\overset{''}{.}0$ (J2000). Details of the map making can be found in Pascale (2011) and Ibar et al. (2010). A catalogue of $\geq 5\sigma$ detections in any of the 250, 350 and 500 μm bands was produced (Rigby et al. 2011) using the MAD-X algorithm (Maddox et al., in preparation) and contains 6876 sources. The 5σ noise levels are 132, 126, 32, 36 and 45 mJy per beam at 100, 160, 250, 350 and 500 μm, respectively; the beam sizes are $\sim$9, $\sim$13, 18, 25 and 35 arcsec in these bands.

The H-ATLAS SDP field overlaps with that of the Galaxy And Mass Assembly (GAMA) survey (Driver et al. 2011; Hill et al. 2011; Robotham et al. 2010; Baldry et al. 2010), which will provide $\sim$350 000 spectra for galaxies at low redshifts over six regions, covering $\sim$300 deg^2. The GAMA data comprise *r*-band defined aperture matched photometry as described in Hill et al. (2011) from UV *GALEX* (Martin et al. 2005; Morrissey et al. 2007, Seibert et al., in preparation), optical *ugriz* Sloan Digital Sky Survey (SDSS) data release 6 (DR6) (Adelman-McCarthy et al. 2008) and near-infrared *YJHK* UKIDSS-LAS (Lawrence et al. 2007) imaging. Spectroscopic redshifts and spectra from the AAOmega spectrograph are provided for $r_{\rm petro} < 19.8$ or ($K_{\rm Kron} < 17.6$ and $r_{\rm modelmag} < 20.5$) or ($z_{\rm Kron} < 18.2$ and $r_{\rm modelmag} < 20.5$)[1] in the G12 field, and $r_{\rm petro} < 19.4$ or ($K_{\rm Kron} < 17.6$ and $r_{\rm modelmag} < 20.5$) or ($z_{\rm Kron} < 18.2$ and $r_{\rm modelmag} < 20.5$) in G15 and G09 which includes the H-ATLAS SDP field.

A likelihood-ratio analysis (Sutherland & Saunders 1992) is performed to match 250 μm sources to SDSS DR7 (Abazajian et al. 2009) sources with $r < 22.4$ within a 10 arcsec radius (Smith et al. 2011a), and accounts for the possibility of the true counterpart being below the optical magnitude limit. The reliability of an association is defined as the probability that an optical source is associated with the submillimetre source. SDSS sources with reliability $\geq$0.8 are considered to be likely matches to submillimetre sources; these are matched to GAMA survey data to provide spectra when available. There are 2423 reliable optical counterparts to H-ATLAS sources, with either photometric or spectroscopic redshifts. Around two-thirds of the objects without reliable optical counterparts are unidentified because their counterparts lie below the optical magnitude limit. These sources mostly reside at $z > 0.5$ (see Dunne et al. 2011). The remaining unidentified sources are believed to have a counterpart in the SDSS catalogue but we are unable to unambiguously identify the correct counterpart in all cases due to near neighbours and the non-negligible probability of a background galaxy of the same magnitude being found at this distance. Smith et al. (2011a) estimate the completeness of the H-ATLAS sample as a function of redshift by calculating the total number of sources that we would expect to have a counterpart above the SDSS magnitude limit in H-ATLAS; we refer the reader to Smith et al. (2011a) and Dunne et al. (2011) for further details. Smith et al. (2011b) find that at $z < 0.35$ the *r*-band selection does not bias our sample towards less obscured sources. Since the majority of our spirals and ETGs lie at redshifts less than this, our sample should be representative of the low-redshift galaxy population. Matches are also made to the *IRAS* (Moshir, Kopman & Conrow 1992) and FIRST radio catalogues (Becker, White & Helfand 1995) as described in Smith et al. (2011a).

[1] $r_{\rm petro}$ is the *r*-band Petrosian magnitude, measured using a circular aperture of twice the Petrosian radius, which is defined using the light profile of the galaxy. $r_{\rm modelmag}$ is the SDSS *r*-band model magnitude, which is determined from the best fit of an exponential or de Vaucouleurs profile; further details are presented in Baldry et al. (2010).

Table 1. Morphologies obtained by visual classification of 1087 H-ATLAS sources and 1052 control sample galaxies. The control sample galaxies are selected to have the same *r*-band magnitude and redshift distribution as those detected in H-ATLAS. The estimated detection fraction of galaxies in each morphological class is shown in the last row. These are estimated as explained in Section 2.1.2.

	Early-type	Late-type	Merger	Unknown
All (detected) 1087	44, 4.1 per cent	496, 45.6 per cent	23, 2.1 per cent	524, 48.2 per cent
All (non-detected) 1052	233, 22.1 per cent	378, 35.8 per cent	22, 2.1 per cent	419, 39.8 per cent
H-ATLAS detected fraction	5.5 per cent	28.2 per cent	25.0 per cent	20.6 per cent

2.1 Morphology

Morphological classification of sources was performed by eye using SDSS standard depth *gri* composite images, and objects were assigned one of four categories: early-type, late-type, merger and unknown. The classification fractions are shown in Table 1. ETGs were identified by looking for a dominant bulge and a complete lack of spiral arms, and late-types were identified by the presence of spiral arms. Due to the shallow depth of the SDSS images, we do not discriminate between E and S0 types; however, it is possible that these populations may have different properties (e.g. Temi, Brighenti & Mathews 2009a). The merger category contains systems of galaxies that are clearly interacting. Galaxies were classified as 'unknown' if it was impossible to assign a morphology, usually because the galaxy was too faint or small. This situation becomes more common as spatial resolution and signal-to-noise ratio decrease at higher redshifts. It is possible that at low redshifts some of the unknown classifications are irregulars, which tend to have small angular size and are therefore difficult to identify. Additionally, very few H-ATLAS galaxies are low stellar mass objects, which is due to the flux limit in the submillimetre. Therefore the dearth of irregulars is likely to be a real effect and not an inability to classify them. Given the sample size, visual inspection is the preferred method to classify our galaxies into broad morphological classes. It has been shown that visual inspection is superior in identifying contaminants in samples of ETGs (e.g. face-on spirals which have a dominant bulge but have weak spiral arms) than automated classification methods (Kaviraj et al. 2007; Schawinski et al. 2007a; Lintott et al. 2008; Bamford et al. 2009). Since we are interested in selecting spheroids, inclination is not an issue. It is possible that at higher redshifts Sa-type galaxies with faint spiral arms not visible in the shallow imaging could be classified as ETGs.

2.1.1 H-ATLAS sample

We morphologically classify 1087 H-ATLAS sources which have reliability $\geq$0.8 of being associated with an SDSS source, and which have good quality spectroscopic redshifts [flagged with z_quality (nQ) $\geq$ 3]. Additionally, we require that sources are at a redshift of $z < 0.5$; above this redshift only a very small number of galaxies have spectroscopic redshifts and will be difficult to classify. Two sources with stellar or quasi-stellar object (QSO) IDs were removed from the sample, as were the five sources identified as being lensed in Negrello et al. (2010). We calculate the number of false IDs expected in the classified sample from the sum of the probabilities of a false ID as $\sum(1 - R)$, where R is the reliability. This indicates that 21 galaxies (2 per cent) in our sample are likely to be false IDs. There are 115 and 199 sources for which we have PACS 100 and 160 μm point-source detections at $\geq 5\sigma$, respectively. The selection effects arising from the PACS detections are discussed in Smith et al. (2011b), who found that the SED results in Section 3 are not significantly influenced by the inclusion of upper limits for PACS data in the majority of the sample. All sources are detected at 250 μm at $\geq 5\sigma$ (which is a requirement for our sample selection), 272 sources have a $\geq 5\sigma$ detection at 350 μm and 138 sources have a $\geq 3\sigma$ detection at 500 μm. The distribution of 100 μm PACS and 250 μm SPIRE detections is shown for each morphological type in Figs 1(a) and (b).

We visually classify 44 galaxies as early-type (E or S0), with $0.01 < z < 0.32$. It can be seen from Table 1 that there are few ETGs in our sample compared to spirals, so it is evident that H-ATLAS preferentially selects spiral galaxies over ETGs. This is as expected since ETGs are generally passive and have little dust content. The late-type category in principle encompasses both spirals and irregular galaxies; however no irregular galaxies are found in our sample. This may be because these objects are difficult to classify at all but the very lowest redshifts, but H-ATLAS also does not detect many low optical luminosity (and therefore low-mass) sources in the SDP field (Dariush et al. 2011; Dunne et al. 2011). The number of mergers in our classified sample is underestimated because the reliability $\geq$0.8 criteria inherently assume a 1:1 correspondence between optical and submillimetre sources (Sutherland & Saunders 1992; Smith et al. 2011a). In the case of mergers there can be two optical sources close to the SPIRE position which both have a high likelihood of association but the probability (reliability) is split between the sources, sometimes reducing the reliability below our threshold of 0.8. The median redshifts of the ETGs and spirals in our sample are both ∼0.13, and the redshift distribution is shown in Fig. 1(c). As galaxies become faint and small with increasing redshift, classification becomes difficult, and the unknown fraction increases significantly for $r_{\rm petro} > 18.5$ (see Fig. 1d). It also seems easier to classify spirals than ETGs at fainter *r*-magnitudes. We observe morphological disturbances in 13/44 (30^{+8}_{-6} per cent) ETGs and 22/496 (4 ± 1 per cent) spirals.[2] These galaxies show evidence of dust or tidal features which may be signs of a merger remnant; however this is a lower limit on the number which may be disturbed since faint features may not be visible in standard depth SDSS images. Morphologically disturbed sources occupy a range of redshifts up to $z \sim 0.26$. We find a higher fraction of morphological disturbance in ETGs compared to Kaviraj (2010) who find 18 per cent for a sample of optically selected ETGs (with $r < 16.5$ and $z < 0.05$).

To check our ETG classifications, we compare to those in the Galaxy Zoo sample (Lintott et al. 2008, 2011), in which galaxies were visually classified by over 100 000 volunteers. Only the brighter members of our H-ATLAS sample ($r < 17.77$ and $z < 0.25$) overlap with Galaxy Zoo. Galaxies were classified as either

[2] The errors are 1σ confidence intervals on a binomial population using a beta distribution, which is appropriate for small population numbers (Cameron 2011).

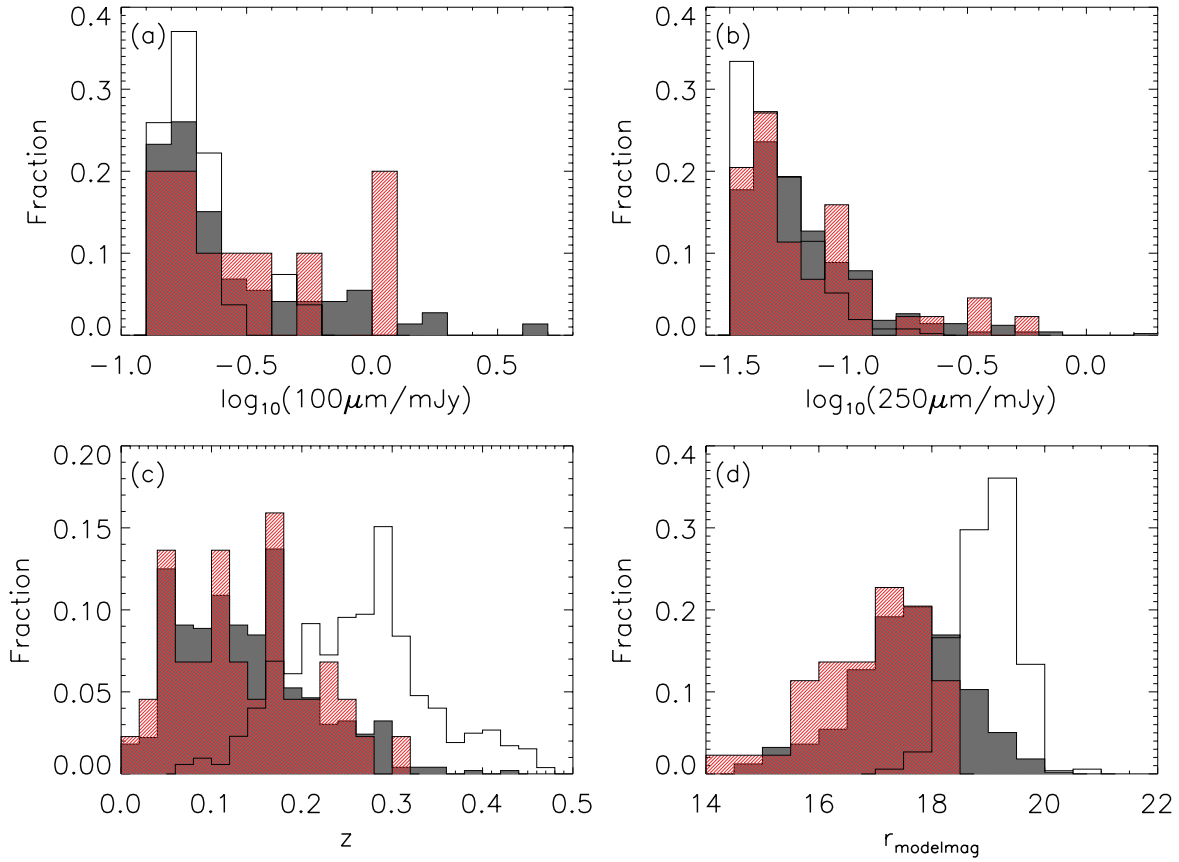

Figure 1. The distribution of $\geq 5\sigma$ 100 μm (a) and 250 μm point-source fluxes (b) is shown for the H-ATLAS morphologically classified sample. Spirals are shown as grey/filled, ETGs as red/hatched and unknown morphologies as an open histogram. It can be seen that the flux distributions are similar for each type of morphology. (c) Redshift distribution of our H-ATLAS sample for each morphological type. The ETGs and spirals have similar redshift distributions, but galaxies classified as unknown lie at much higher redshift on average. (d) The distribution of SDSS *r*-band model magnitudes for the same morphological classifications. Sources with unknown morphologies are fainter on average than those which are classified.

elliptical,[3] spiral, merger or 'don't know'. We assign a galaxy one of these classifications if it has >50 per cent of the vote fraction. Debiased votes are used to account for the tendency for Galaxy Zoo classifiers to assign small or faint galaxies (usually at higher redshift due to a lack of resolution) to the 'elliptical' category. The debiasing procedure is described fully in Bamford et al. (2009) and Lintott et al. (2011). There are 22 of our ETGs which have a match in Galaxy Zoo, 17/22 are classified as elliptical, 3/22 are classified as spiral and two are ambiguous. The ETGs which are classified as spirals in Galaxy Zoo either have evidence of disturbed morphology which could have been mistaken for spiral structure or have evidence of a disc yet no spiral arms. The majority of our H-ATLAS ETGs which match with the Galaxy Zoo sample are classified as 'elliptical', and so our morphological classifications agree well with overlapping studies.

We also examine the Sérsic index (n) of our ETGs and spirals in Fig. 2, to check that our morphological classifications are broadly consistent with what is expected from automated galaxy classification. This is accomplished by fitting single component Sérsic models to the light profile of the galaxy (Kelvin et al., in preparation). Generally, late-type galaxies have an exponential profile ($n = 1$), and ETGs have a de Vaucouleurs profile ($n = 4$). As expected, our visually classified spirals have a very strong peak at

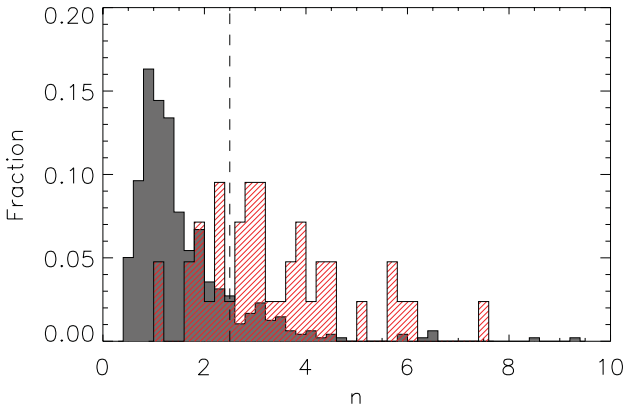

Figure 2. The Sérsic index (n) distribution of the spirals (grey), and ETGs (red/hatched) in our H-ATLAS sample. The dashed line at $n = 2.5$ denotes the traditional cut between 'early-type' ($n > 2.5$) and 'late-type' ($n < 2.5$), and gives an indication of the contamination that can occur in samples selected on the Sérsic index.

$n = 1.3$, whereas the ETGs have a variety of Sérsic indices, but have a higher average n of 3.1. The wide range of Sérsic indices is because we include S0s in our early-type classification, which may have a substantial disc component. We note that although n broadly agrees with our visual morphologies, the Sérsic index is not the ideal classification method, because a spiral with a bright nucleus may

[3] The 'elliptical' classification also contains the majority of S0 galaxies, as shown in Bamford et al. (2009).

appear to have a high value of n and would be misclassified as an ETG (e.g. Bamford et al. 2009).

2.1.2 Control sample

In order to understand how the H-ATLAS and optically selected ETG populations differ, we obtain visual morphological classifications of a control sample drawn from the GAMA galaxy catalogue which overlaps with the H-ATLAS SDP field. Galaxies are required to be undetected in H-ATLAS and have good quality spectroscopic redshifts, and were chosen to have the same redshift and $r_{\rm petro}$ - magnitude distribution $n(r, z)$ as our H-ATLAS detected, morphologically classified sample. This was accomplished by splitting the H-ATLAS sample into (r, z) bins, and randomly picking approximately the same number of galaxies in each bin from the GAMA catalogue, so that the control sample comprises 1052 galaxies. By selecting a control sample of galaxies which are matched in redshift to the H-ATLAS sample, we avoid selection effects.

The morphologies of the control sample are summarized in Table 1. It can be seen that there are many more ETGs compared to spirals in the optically selected sample than in the 250 μm selected sample. To estimate the fraction of galaxies which are detected at the depth of H-ATLAS as a function of morphology, we pick a random sample of 1076 galaxies[4] from the GAMA catalogue in the SDP field, disregarding whether they are detected by *Herschel*. We make sure the selected galaxies follow the same $n(r, z)$ as our H-ATLAS detected and control samples. We repeat the random sampling 1000 times to estimate the average number of H-ATLAS detected and undetected galaxies. On average, 225 galaxies are in the H-ATLAS detected sample, and 11 of these are ETGs. There are 851 undetected galaxies, and from the control sample fractions we expect 22 per cent (188) of these to be ETGs. Consequently, there are 199 ETGs in total in the random sample, so we estimate 5.5 per cent of ETGs are detected in H-ATLAS compared to the total number of ETGs in the SDP field, for this $n(r, z)$. The detected fractions of other morphological types are presented in Table 1. We cannot reliably extrapolate the control sample fractions to the entire SDP field, since morphology is a function of both r and z, and we have not probed the full (r, z) parameter space in this work.

2.1.3 Classification bias

Bamford et al. (2009) showed that in Galaxy Zoo the fraction of galaxies classified as 'elliptical' increases with redshift compared to spirals. This is because the spatial resolution and signal-to-noise ratio decrease with redshift, so features such as spiral arms become invisible. Also, in Galaxy Zoo, images are presented to the classifier without any indication of angular scale, so distant, unresolved galaxies could have been classified as elliptical. We should therefore check if this bias is present in our classifications. We show the classification fractions of our H-ATLAS sample in Fig. 3, and there is no trend that we classify more ETGs with increasing redshift. Indeed, we see that we classify fewer. This may be because unlike Galaxy Zoo volunteers, our expert classifier recognizes the limitations of the resolution of the image, and will classify an object as unknown instead of as an ETG.

[4] The random sample is chosen to be approximately of the same size as the H-ATLAS detected sample, but 11 H-ATLAS galaxies are not in the GAMA survey region and lack $r_{\rm petro}$-magnitude information. Therefore, the size of the random sample is smaller than the H-ATLAS sample, but this should not affect any of our conclusions.

2.2 SED fitting

Smith et al. (2011b) fit the UV-submillimetre SEDs of 1404 H-ATLAS galaxies with reliability >0.8 of being associated with an optical counterpart in the SDSS r-band catalogue, and which have available multiwavelength photometry. Using the physically motivated method of da Cunha, Charlot & Elbaz (2008, hereafter DCE08) allows us to recover the physical properties of these galaxies. In this method the energy from UV-optical radiation emitted by stellar populations is absorbed by dust, and this is matched to that re-radiated in the FIR. Spectral libraries of 25 000 optical models with stochastic star formation histories, and 50 000 infrared models, are produced at the redshift of each galaxy in our sample, containing model parameters and synthetic photometry from the UV to the submillimetre. The optical libraries are produced using the spectral evolution of stellar populations using a Chabrier (2003) Galactic-disc initial mass function (IMF), calculated from the latest version of the population synthesis code of Bruzual & Charlot (2003), which includes a revised prescription for thermally pulsing asymptotic giant branch (TP-AGB) stars (Bruzual & Charlot, in preparation). These libraries contain model spectra with a wide range of star formation histories, metallicities and dust attenuations. The two-component dust model of Charlot & Fall (2000) is used to calculate the attenuation of starlight by dust, which accounts for the increased attenuation of stars in birth clouds compared to old stars in the ambient interstellar medium (ISM). The model assumes angle averaged spectral properties and so does not include any spatial or dynamical information.

The infrared libraries contain SEDs with different temperature dust components, which include polycyclic aromatic hydrocarbons (PAHs), hot dust (stochastically heated small grains, 130–250 K), warm dust in birth clouds (30–60 K) and cold dust grains (15–25 K) in thermal equilibrium in the diffuse ISM, from which the dust mass ($M_{\rm d}$) is calculated. A dust emissivity index $\beta = 1.5$ is assumed for warm dust, and $\beta = 2.0$ for cold dust, as described in DCE08.

The attenuated stellar emission and dust emission models in the two spectral libraries are combined using a simple energy balance argument: that the energy absorbed by dust in stellar birth clouds and the diffuse ISM are re-emitted by dust in the infrared. In practice, this means that each model in the optical library is matched to models in the infrared library which have the same value of f_{μ}(within a tolerance of 0.15) and are scaled to the total dust luminosity[5] $L_{\rm d}^{\rm tot}$. We derive statistical constraints on the various parameters of the model using the Bayesian approach described in DCE08. We compare each observed galaxy SED to the library of stochastic models which encompasses all plausible parameter combinations. For each galaxy, we build the marginalized likelihood distribution of any physical parameter by evaluating how well each model in the library can account for the observed properties of the galaxy (by computing the χ^2 goodness of fit). This method ensures that possible degeneracies between model parameters are included in the final probability density function (PDF) of each parameter. The effects of individual wavebands on the derived parameters are explored in DCE08 and Smith et al. (2011b), but we emphasize the importance of using the H-ATLAS FIR-submillimetre data to sample the peak of the dust emission and the Rayleigh–Jeans slope in order to get reliable constraints on the dust mass.

An example best-fitting SED and set of PDFs are shown in Fig. 4. The parameters we compute are f_{μ}, the fraction of total dust

[5] Integrated between 3 and 1000 μm.

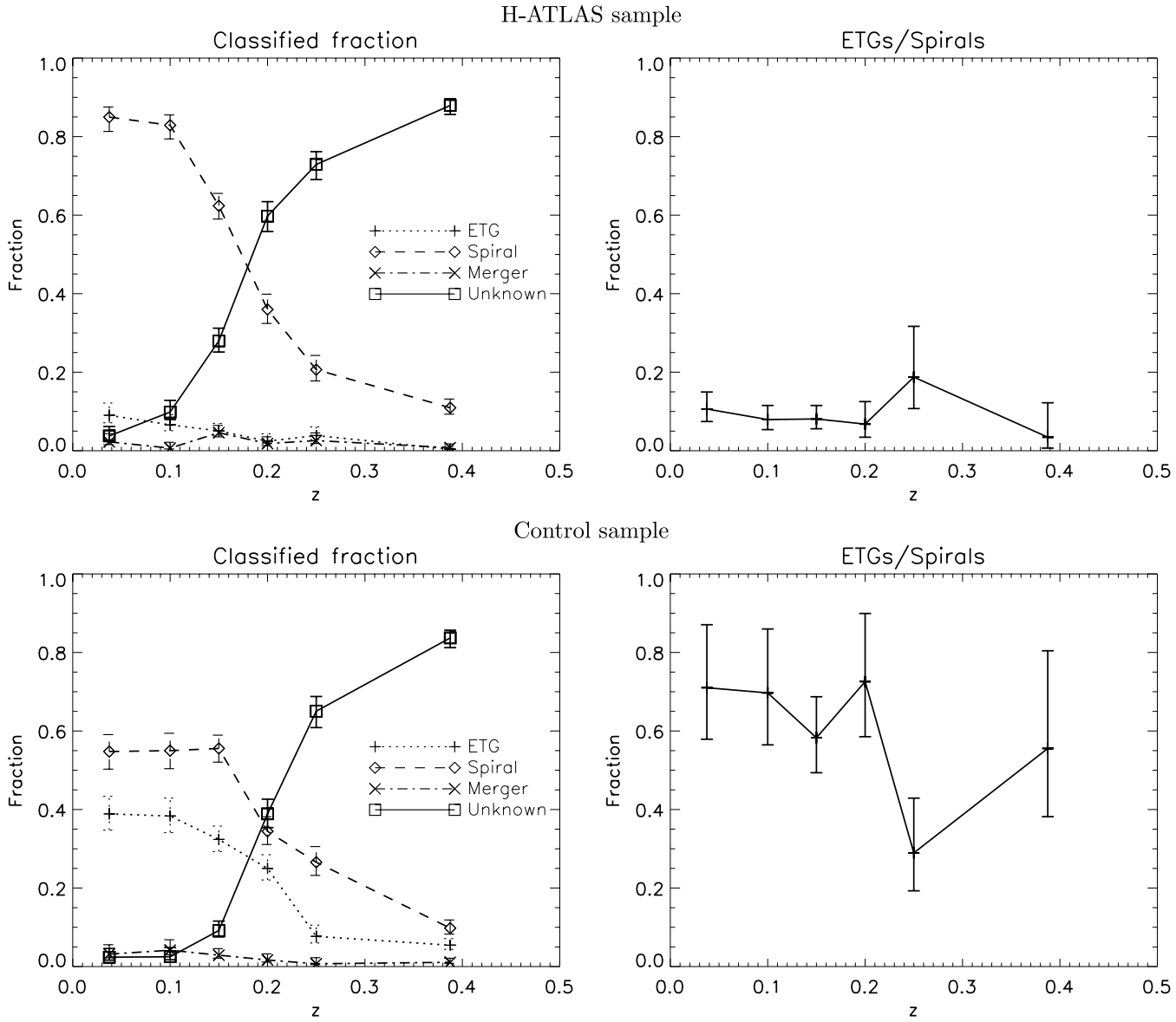

Figure 3. Morphological classification fractions as a function of redshift for the H-ATLAS detected sample (top) and the control sample (bottom). Error bars are the 1σ confidence intervals for a binomial population, derived from a beta distribution (see Cameron 2011). Also shown is the ETG-to-spiral fraction for both samples, where error bars are the 1σ confidence intervals for a binomial distribution, using the approximation of Gehrels (1986). The ETG-to-spiral fraction does not increase with redshift, therefore we do not observe a bias towards classifying more ETGs as they become smaller and fainter.

luminosity contributed by the diffuse ISM; $\hat{\tau}_V$, total effective V-band optical depth seen by stars in birth clouds; $M_*/\mathrm{M}_\odot$, stellar mass; $L_\mathrm{d}^\mathrm{tot}/\mathrm{L}_\odot$, dust luminosity; $T_\mathrm{C}^\mathrm{ISM}/\mathrm{K}$, temperature of the cold diffuse ISM dust component; $\hat{\tau}_V^\mathrm{ISM}$, the V-band optical depth in the ambient ISM; $M_\mathrm{d}/\mathrm{M}_\odot$, dust mass; $\psi_\mathrm{S}/\mathrm{yr}^{-1}$, specific star formation rate (SSFR); $\psi/\mathrm{M}_\odot\mathrm{yr}^{-1}$, SFR; t_LB, time of last burst; age$_r$, r-band light-weighted age and M_d/M_*, dust-to-stellar mass ratio. For more details of the method we refer the reader to DCE08.

3 PROPERTIES OF ETGS COMPARED TO SPIRALS

Here we explore the multiwavelength properties of our sample of morphologically classified spirals and ETGs detected in H-ATLAS. We present parameters derived from the SED fitting method as described in Section 2.2 for 42 of the 44 ETGs, and as a comparison we also explore the properties of 450 out of the 496 spiral galaxies in our sample. We present the SDSS images, best-fitting SEDs and optical spectra of these ETGs in Fig. A1 and physical properties in Table A1. The galaxies which are excluded from our analysis do not have available aperture-matched GAMA photometry (two ETGs, 17 spirals); additionally we reject 29 galaxies from our analysis which have poor quality SED fits with $\chi^2 > 30$. Our sample covers a range of redshifts, but since the median redshifts of the ETGs and spirals are approximately the same, differences between the samples due to evolution in the redshift range are likely to be small. Additionally, we have checked that the following trends are present if we look at galaxies at $z < 0.13$, and $z > 0.13$. We also observe similar results if we separate our successfully classified sample into 'early-type' ($n > 2.5$) and 'late-type' ($n < 2.5$) using the Sérsic index.

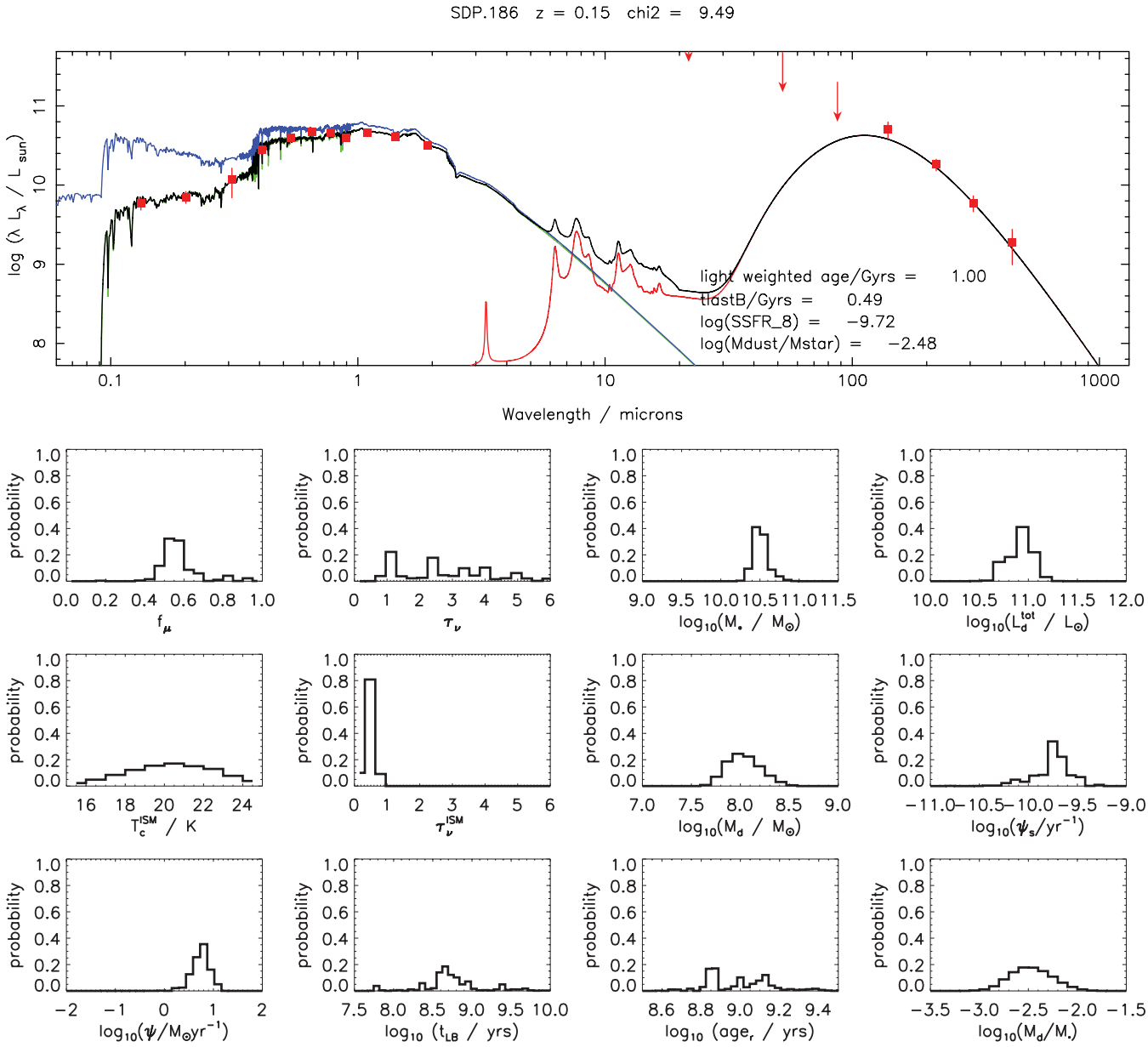

Figure 4. Top: example best-fitting rest-frame SED of an ETG, with observed photometry points from the UV to the submillimetre (red squares). 5σ upper limits are shown as arrows. Errors on the photometry are described in Smith et al. (2011b). The black line is the best-fitting model; the green line is the attenuated optical model; the blue line is the unattenuated optical model and the red line is the infrared model. Bottom: PDFs of parameters for this ETG.

3.1 SED parameters

In order to compare physical parameters for ETGs and spirals in our sample, we compute the average PDF of parameters derived from our SED fitting. The average PDFs of ETGs (red) and spirals (black) are shown in Fig. 5, and the mean values and errors are summarized in Table C1. For each parameter, we use the first moment of the average PDF to estimate the mean of the population. We can estimate the variance on the population mean as the second moment of the average PDF minus the mean squared, divided by the number of galaxies in the sample. The error on the mean is simply the square root of the population variance. The significance of the difference in the means is shown in brackets in Fig. 5 and uses the quadrature sum of the errors on the mean for the two populations.

The ETGs have a mean f_μ of 0.74 ± 0.02, which is significantly higher than that of spirals which have a mean f_μ of 0.59 ± 0.01. This means that most of the FIR luminosity in ETGs is from dust in the diffuse ISM, which is mostly heated by old stellar populations (stars older than 10^7 yr). Some ETGs have lower values of f_μ, indicating that more of the FIR luminosity comes from dust in birth clouds, which is heated by young stars and implies ongoing star formation. The ETGs in our sample are more massive than spirals, with ETGs having a mean stellar mass (M_*) of $(4.9^{+1.0}_{-0.8}) \times 10^{10}$ M$_\odot$ compared to M_* of $(1.9 \pm 0.1) \times 10^{10}$ M$_\odot$ for spirals. ETGs have approximately the same mean dust mass (M_d) and dust luminosity ($L_\mathrm{d}^\mathrm{tot}$) as spirals, although the mean ratio of dust to stellar mass (M_d/M_*) for ETGs is lower than that for spirals in our sample by 0.38 dex, meaning that ETGs are dust deficient for their stellar mass

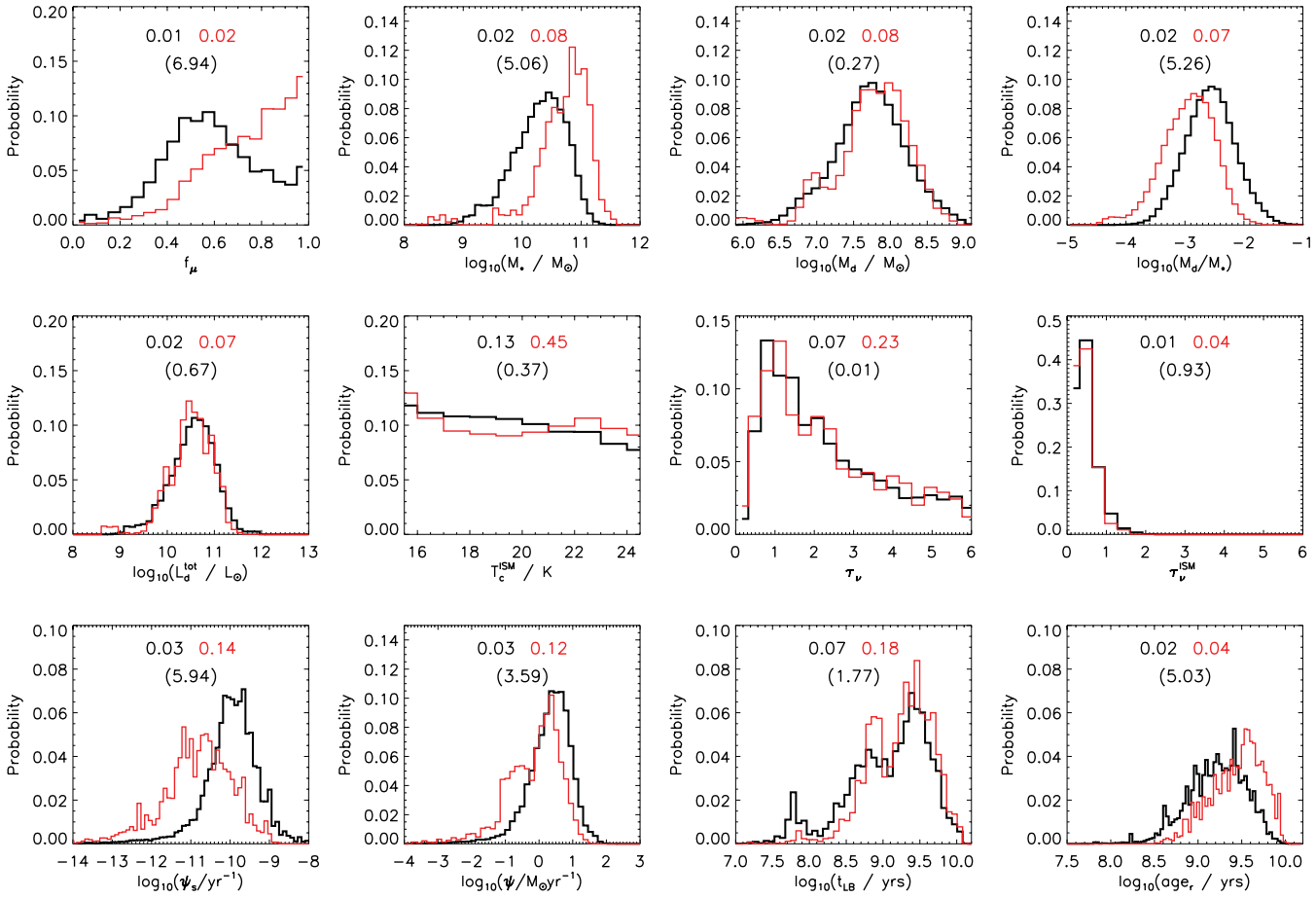

Figure 5. Average PDFs of the SED parameters of 42 ETGs (red line) compared to 450 spirals (black line). The parameters are (from left to right): f_μ, the fraction of total dust luminosity contributed by the diffuse ISM; M_*, stellar mass; M_d, dust mass; M_d/M_*, dust-to-stellar mass ratio; $L_\mathrm{d}^\mathrm{tot}$, dust luminosity; $T_\mathrm{C}^\mathrm{ISM}$, temperature of the cold ISM dust component; $\hat{\tau}_V$, total effective V-band optical depth seen by stars in birth clouds; $\hat{\tau}_V^\mathrm{ISM}$, the V-band optical depth in the ambient ISM; SSFR and SFR averaged over the last 10^8 years; t_LB, time of last burst; and age$_r$, the r-band light-weighted age of the stellar population. The uncertainty on each distribution for ETGs and spirals is given by the error on the mean and is shown at the top of each histogram with corresponding colours, and the significance of the difference in the means in brackets. The errors for logarithmic parameters are in dex.

compared to spirals. Our median M_d/M_* value for ETGs is $(1.6 \pm 0.1) \times 10^{-3}$, which is larger than the average found by Skibba et al. (2011) of 1.7×10^{-4} for 10 ETGs. In order to contain enough dust to be detected in H-ATLAS, galaxies which have low M_d/M_* need to be more massive in general, which may explain why ETGs have a higher M_* on average than spirals in our sample. We find a mean dust mass of $(5.5^{+1.1}_{-0.9}) \times 10^7\,\mathrm{M}_\odot$ for the sample of ETGs, which is larger than the highest dust masses found in some previous studies of ETGs; e.g. Temi et al. (2004) found 10^5–$10^7\,\mathrm{M}_\odot$, which is similar to the dust masses found in ETGs with optical dust lanes (Kaviraj et al. 2011b) (although these are likely to be underestimated by the use of *IRAS* data, this issue will be addressed in future work). Our mean dust mass is consistent with Vlahakis et al. (2005) who found dust masses greater than $10^7\,\mathrm{M}_\odot$ for six elliptical galaxies from an optically selected sample observed with SCUBA. The dust mass inferred for the SCUBA ellipticals may include contamination from synchrotron radiation, but for the sample of ETGs studied here, we find that synchrotron radiation is negligible compared to thermal emission from dust (see Section 5.3). We find no significant difference in the $T_\mathrm{C}^\mathrm{ISM}$ of the spirals and ETGs, and find a wide range of values for the dust temperature. The total effective V-band optical depth seen by stars ($\hat{\tau}_V$, $\hat{\tau}_V^\mathrm{ISM}$) is approximately the same for ETGs and spirals. This shows that ETGs have approximately the same attenuation as spiral galaxies (though with rather large uncertainties).

3.2 Star formation histories

We investigate the SFH of our galaxies by examining the SFR, (ψ) and SSFR, (ψ_S, defined as ψ/M_*) averaged over the last 10^8 yr. These parameters are derived from the SED fitting as described in Section 2.2. The model SFHs are described by a continuous exponentially decreasing SFR, with superimposed randomly distributed bursts of star formation (Kauffmann et al. 2003a) lasting between 3×10^7 and 3×10^8 yr. These bursts occur with equal probability throughout the lifetime of the galaxy. The probability is set such that 50 per cent of the galaxies in the library have undergone a burst of star formation in the last 2 Gyr. The amplitude of the burst (ratio of mass formed in the burst to mass formed in continuous star formation over the lifetime of the galaxy) is distributed logarithmically between 0.03 and 4.0. For further details of the models, and the effects of model assumptions on derived parameters we refer the reader to Kauffmann et al. (2003a) and DCE08.

The mean SFR for ETGs is $0.7 \pm 0.2\,\mathrm{M}_\odot\,\mathrm{yr}^{-1}$, with a range of 0.04–$12.4\,\mathrm{M}_\odot\,\mathrm{yr}^{-1}$. It is interesting to note that the distribution

of ETG SFRs in Fig. 5 shows signs of bimodality. Our range of SFRs is comparable to that found for optically blue ETGs by Schawinski et al. (2009), who find SFRs of 0.5–50 $M_\odot$ yr^{-1} using a range of indicators (Hα luminosity, *u*-band light, infrared luminosity from *IRAS*). H-ATLAS ETG SFRs are also larger than those found in recent studies of ETGs in the SAURON sample, which is a representative sample of local ETGs located in both clusters and the field (de Zeeuw et al. 2002). Temi et al. (2009a) find that the SFR for SAURON S0s as estimated from 24 μm luminosity is 0.02–0.2 $M_\odot$ yr^{-1}, and Shapiro et al. (2010) calculated the SFR in the SAURON sample from non-stellar 8 μm emission, and this was found to be $<0.4\,M_\odot$ yr^{-1}. These findings of low level star formation in the SAURON galaxies can possibly be explained by the optical selection, which is not biased towards highly star-forming galaxies. This is in contrast to the H-ATLAS sample which selects the dustiest ETGs, and therefore the highest SFRs. Additionally, the SAURON measurements only give the obscured SFR, and may not be representative of the total SFR of the galaxy.

SSFR is defined as the star formation rate per unit stellar mass and measures the star formation efficiency of a galaxy. Fig. 5 shows that the mean SSFR averaged over the last 10^8 yr for ETGs ($1.4^{+0.5}_{-0.3} \times 10^{-11}$ yr^{-1}) is lower than that of spirals ($1.0 \pm 0.7 \times 10^{-10}$yr^{-1}). This trend is insensitive to changes in the time-scale over which the SSFR is averaged. There is, however, a wide range of SSFR and 17 per cent of ETGs have a SSFR greater than the mean of the spiral sample.

In Fig. 6(a), we show a plot of dust mass versus SFR for spirals and ETGs in our sample. It can be seen that galaxies with the highest dust mass also have a high SFR. This trend is expected since both dust mass and SFR will depend on the total stellar mass of a galaxy. We can remove this trend by dividing by stellar mass and so we plot M_d/M_* versus SSFR in Fig. 6(b). As was found in da Cunha et al. (2010), there is a strong correlation between these two parameters. It can be seen that typically the ETGs have lower SSFR and M_d/M_* than spirals. There are some spirals with very low SSFR and M_d/M_*, which are discussed in Section 4.

We can use the results of our SED fitting to see if star formation is dominated by a recent burst or continuous star formation using the model parameter t_{LB}. Although there is a large uncertainty on this parameter, our results are still useful for a statistical comparison of two populations. As shown in Fig. 5, ∼76 per cent of our ETGs have not had a burst of star formation in the last 10^9 yr, and have therefore not formed a substantial fraction of their mass in recent bursts. It seems that most of our sample have residual star formation left over from the last major burst. Kauffmann et al. (2003b) find that galaxies with $M_* > 10^{10}\,M_\odot$ typically have not had recent bursts of star formation, which may explain why our generally high mass ETG sample shows few recent bursts. The time since the last burst can also be characterized by the age of the young stellar population, parametrized in our models by the *r*-band light-weighted age (age$_r$). It is found that the mean stellar population age of the ETGs is 2.8 ± 0.3 Gyr, which is older than that found for the spirals of 1.6 ± 0.1 Gyr. This is consistent with the general picture that ETGs are older than spirals. We note that 3/10 ETGs with bursts of star formation in the last 1 Gyr show disturbed morphologies, so galaxy interactions may be the cause of the burst. It is possible that more ETGs in this sample are disturbed at a level which is not detected in the shallow imaging that we have available. Without deeper imaging, conclusions cannot be drawn about whether there is a correlation between morphological disturbance and recent star formation in this sample.

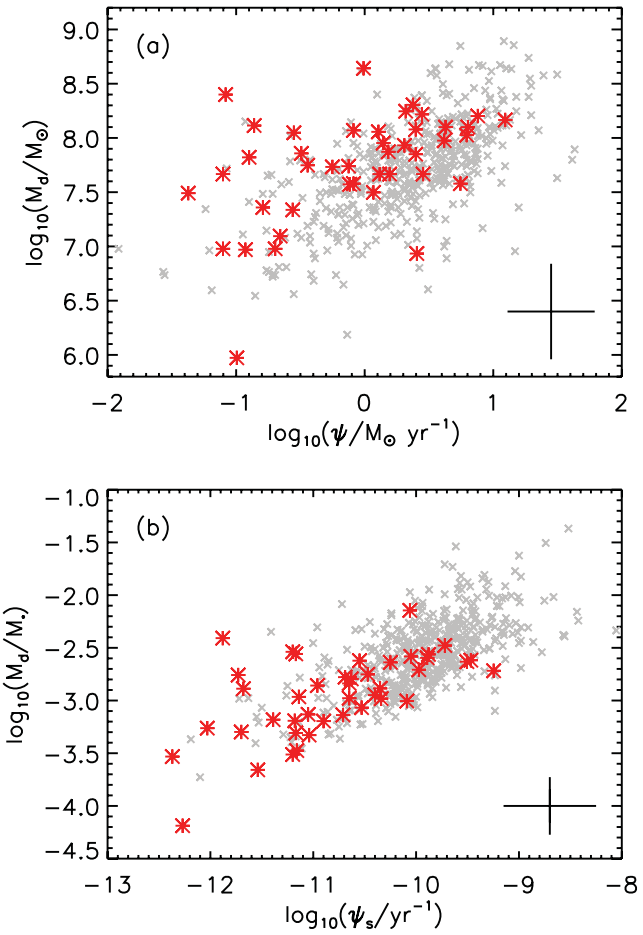

Figure 6. (a) M_d versus SFR of the ETGs (large red stars) compared to the spiral galaxies (small grey crosses). (b) M_d/M_* versus SSFR of the ETGs compared to the spiral galaxies. The error bars indicate the median 1σ uncertainty on a data point.

3.3 Comparison of broad-band photometric and spectroscopic star formation parameters

SFH parameters are traditionally measured using spectroscopic information, whereas we used broad-band data, so there may be a large uncertainty on some parameters. Walcher et al. (2008) explored degeneracies in the SFH parameters from broad-band photometry using similar stellar population models to those in this work, and found that M_*, age$_r$ and ψ_S are well determined. Wild et al. (2009) classify galaxies into star-forming galaxies and quiescent galaxies using broad-band and spectroscopic data, and found a good agreement between these two classification methods. They also find the time of last burst derived from broad-band SED fitting agrees with that derived from spectroscopy.

To investigate whether fitting SEDs to broad-band photometry can accurately describe the SFHs of our galaxies, we stack spectra of ETGs and spirals together in bins of SSFR and *r*-band weighted age to look for trends in spectral features. The spectra are shifted to rest wavelength and resampled on to a common wavelength array. The spectra are normalized to the median of the spectrum, and then combined using the median of the spectra in each bin. Spectra which show signs of AGN (see Section 5), or have anomalous effects such as bad sky subtraction or fibre fringing (Colless et al. 2001), have been removed. It can be seen from Fig. 7 that as expected, the galaxies with the highest SSFR show signatures of star formation

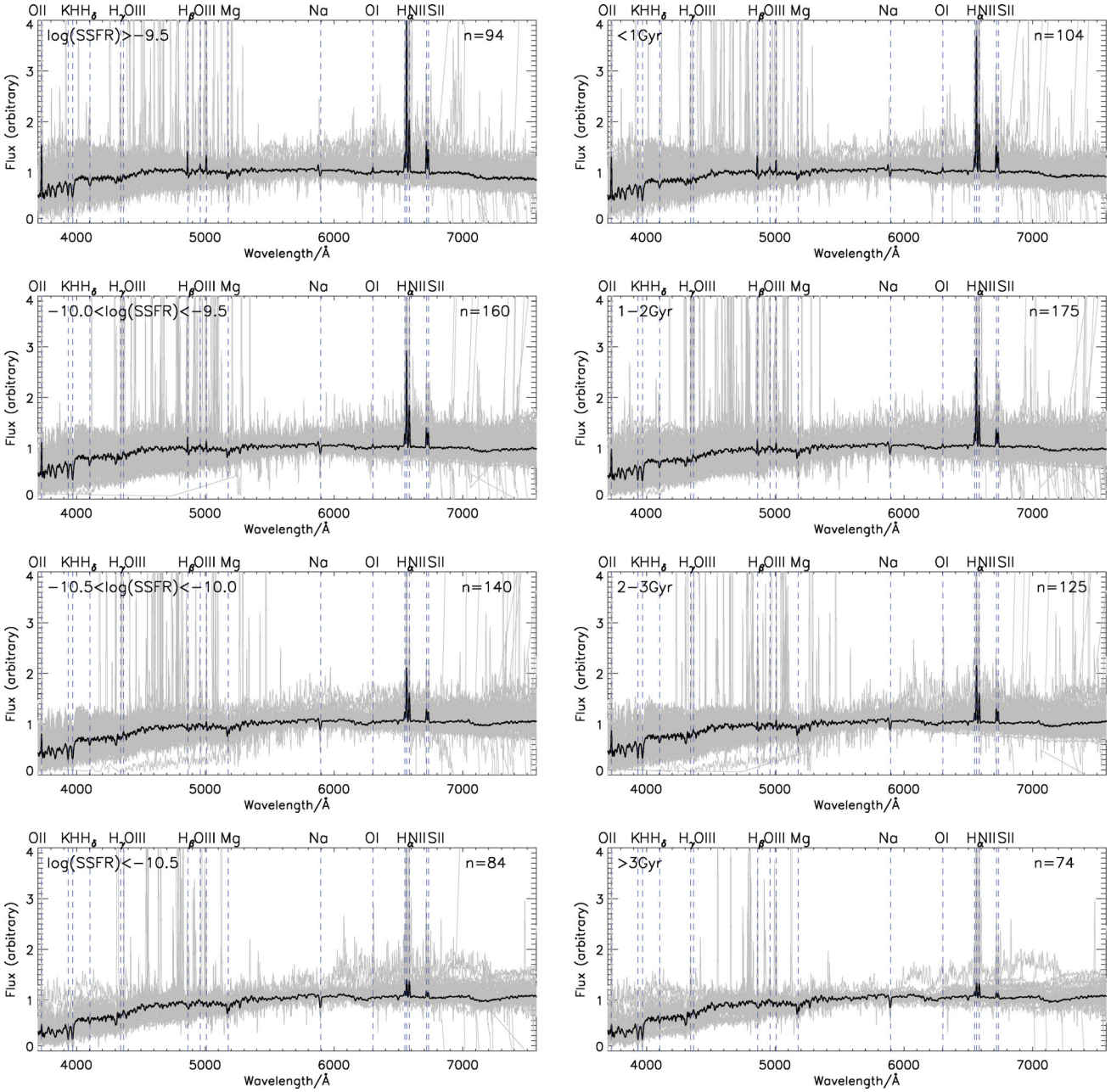

Figure 7. Stacked spectra in bins of SSFR (left) and stellar population age (right). The bins are arranged from high SSFR/young stellar population (top) to low SSFR/old stellar population (bottom). The grey area shows the normalized, individual spectra, and the thick black line is the median of these spectra, smoothed by a boxcar of 5 Å. Prominent emission lines are shown by the blue dashed lines. The number of spectra in each stack is indicated in each panel.

such as strong Hα and [O III] and [O II] emission lines. Going from high to low SSFR, the strength of the emission lines decreases; the same trends are found for age, with older stellar populations showing minimal signs of star formation.

3.4 UV-optical colours

Galaxy colour is often used as a proxy for the age of a stellar population, with red galaxies assumed to be old due to a lack of UV emission from young stars. This simple interpretation can become complicated, with young star-forming galaxies appearing red due to dust obscuration, and old galaxies appearing blue due to contamination of the UV light by horizontal branch stars[6] (O'Connell 1999; Yi et al. 2005; Kaviraj et al. 2009). Dariush et al. (2011) separate red and blue galaxies in the H-ATLAS sample at $NUV - r = 4.5$ by fitting double Gaussians to the colour distribution. They found that *Herschel* preferentially selects blue galaxies, and that 90 per cent of H-ATLAS sources with red colours are not old/passive[7] but have

[6] We note that UV contamination from old stars is unlikely to be a concern, since our sample does not contain giant elliptical galaxies (Yi, Demarque & Oemler 1997), and UV flux from old stars is likely to be swamped by that produced by young stars (Kaviraj et al. 2011).

[7] Dariush et al. (2011) define 'passive' systems as galaxies which have red ($NUV - r > 4.5$) colours, after correcting for dust obscuration.

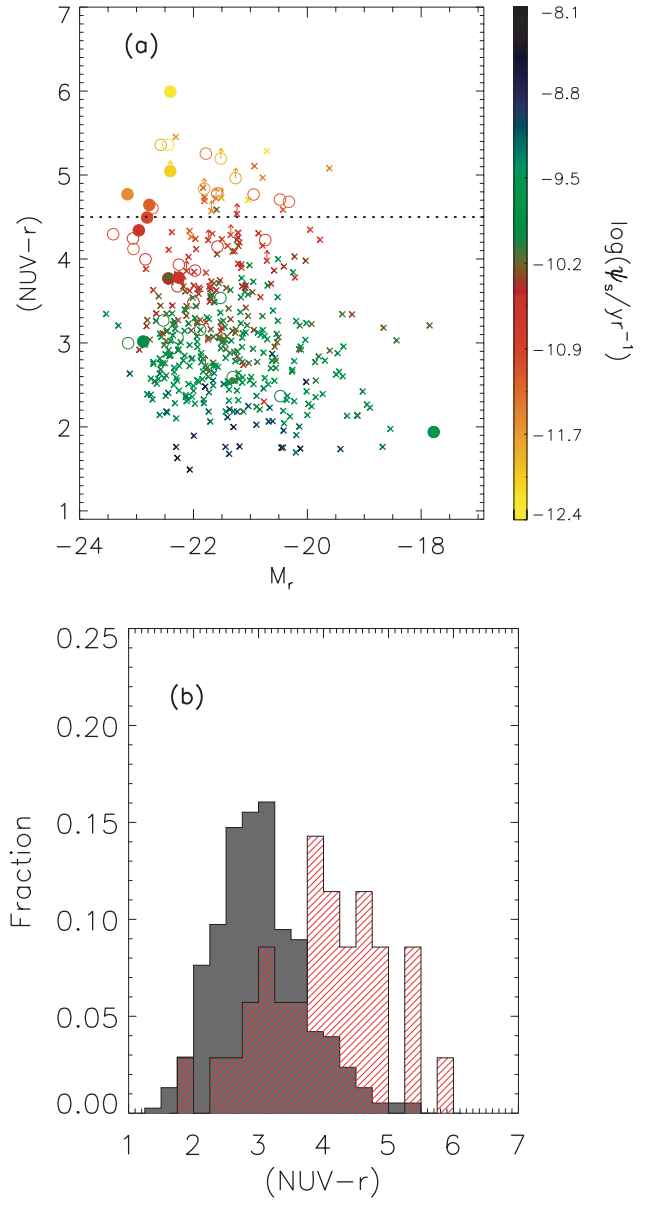

Figure 8. (a) UV-optical colour–magnitude diagram, colour coded according to SSFR. Circles are ETGs, crosses are spirals and filled circles indicate that the ETG is morphologically disturbed. The dashed line shows the separation between 'blue' and 'red' as defined in Dariush et al. (2011). Lower limits are shown for galaxies which do not have a $\geq 5\sigma$ NUV detection. (b) The distribution of ($NUV - r$) colours for the ETGs (red/hatched) and spirals (grey) which have a $\geq 5\sigma$ NUV detection.

their light attenuated by dust. We examine the $NUV - r$ colours of our morphologically selected galaxies using aperture matched *GALEX* UV and GAMA optical photometry in Fig. 8. Rest-frame photometry is calculated using *k*-CORRECT.v4.2 (Blanton & Roweis 2007), and is corrected for galactic extinction using the reddening data of Schlegel, Finkbeiner & Davis (1998). Overall, 93 per cent of ETGs have available NUV photometry. For sources which have a $<5\sigma$ NUV detection,[8] we compute lower limits for the colours. The mean error in the $NUV - r$ colour is 0.08 mag.

[8] Corresponding to $NUV > 23.0$ in the AB magnitude system after galactic extinction correction.

Using the colour cut of Dariush et al. (2011) at $NUV - r = 4.5$ in Fig. 8(a), we find the ETGs have a range of colours, with 24 'blue' and 15 'red' ETGs. Many exist in the transition region between the red sequence and blue cloud. The SSFR of each galaxy is represented by the colour of each point, and a correlation with $NUV - r$ colour is observed. As expected, blue galaxies tend to have a higher SSFR, and red galaxies a lower SSFR, although with some exceptions. In Fig. 8(b) there is a wide range in the colours of both morphological types, although the median $NUV - r$ colour for the spirals is bluer than that of the ETGs. This trend is expected since spirals have the bulk of their stellar population dominated by young stars.

The red ETGs generally have low SSFR, but still contain an appreciable amount of dust. These sources have high f_μ values which indicate the dust in these sources is predominantly heated by an older stellar population, which gives rise to the red colour of these galaxies. We are observing these objects at a time when their star formation has mostly ceased, either because they have used up all their gas, or because star formation has been quenched by some process. Their dust has not yet been destroyed by sputtering and shocks from Type Ia SNe, and this is discussed in Section 8.

The ETGs which show signs of morphological disturbance (denoted by filled circles in Fig. 8a) span a range of colours. A Kolmogorov–Smirnov (KS) test gives a probability of 0.14 of the colours of disturbed and non-disturbed ETGs being drawn from the same distribution; however, this is not significantly different (1.1σ). In contrast, Kaviraj (2010) find that peculiar ETGs have significantly bluer $NUV - r$ colours than relaxed ETGs. There is also a small population of 15 spirals with $NUV - r > 4.5$, and these are discussed in the following section.

4 PASSIVE AND RED SPIRALS

There has been much discussion in the literature about whether the red colour of some spirals is due to dust extinction or an old stellar population (Wolf, Gray & Meisenheimer 2005; Wolf et al. 2009; Masters et al. 2010b). Wolf et al. (2009) find optically red spirals have a lower SFR than blue spirals, but also contain large amounts of dust which obscures star formation. This may be due to the inclusion of edge-on spirals in their sample, which would inherently have a higher dust extinction because the central dust lane is oriented along our line of sight.

Of the 15 red ($NUV - r > 4.5$) spirals in our sample, only two have moderate levels of star formation with SSFR $\geq 10^{-11}\,\mathrm{yr}^{-1}$. The majority of the red spirals have SSFR much lower than this. By selecting spirals with SSFR $< 10^{-11}\,\mathrm{yr}^{-1}$ we explore the properties of the 19 ($\sim$5 per cent) most passive galaxies in our spiral sample. We note that this is different from the 'passive' definition used by Dariush et al. (2011), which was based on dust-corrected UV-optical colour. The error on the SSFR for some passive spirals is large (up to 2.1 dex), meaning that some passive spirals could plausibly have SSFR $> 10^{-11}\,\mathrm{yr}^{-1}$; however, the mean of the average SSFR PDF is $(2.6^{+1.3}_{-0.9}) \times 10^{-12}\,\mathrm{yr}^{-1}$. As a population, we can regard the average SSFR of passive spirals as being significantly (9.3σ) different from those of normal spirals [which have a mean of $(1.2 \pm 0.1) \times 10^{-10}\,\mathrm{yr}^{-1}$]. SDSS images, best-fitting SEDs and optical spectra of the passive spirals are presented in Fig. B1.

These spirals have $NUV - r$ colours ranging from 4.3 to 5.5, although there are 2/19 spirals for which NUV magnitudes are not measured due to the source being in close proximity to a bright star. We find 13/17 passive spirals are 'red', and 3/17 are 'blue', with one passive spiral having ambiguous colour due to an upper limit

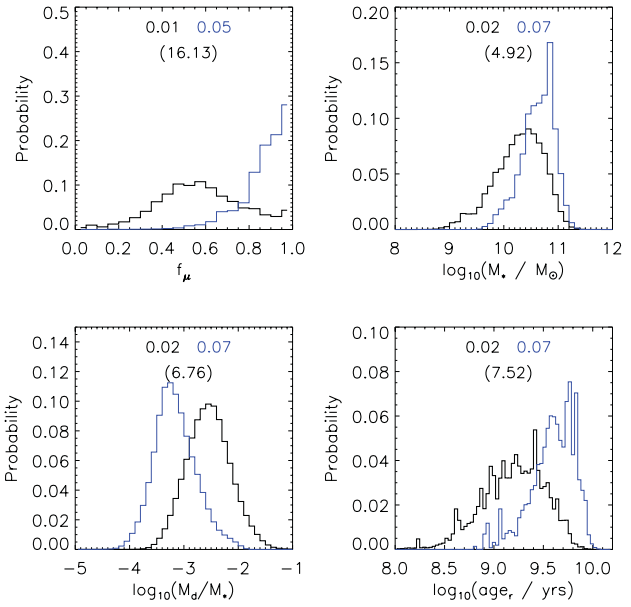

Figure 9. Average PDFs of the SED parameters of 19 passive spirals (SSFR $< 10^{-11}$ yr^{-1}) (blue line) compared to 431 normal spirals with SSFR $\geq 10^{-11}$ yr^{-1} (black line). The parameters are (from left to right): f_μ, the fraction of total dust luminosity contributed by the diffuse ISM; M_*, stellar mass; M_d/M_*, dust-to-stellar mass ratio; and age$_r$, the r-band light-weighted age of the stellar population. The uncertainty on each distribution for ETGs and spirals is given by the error on the mean and is shown at the top of each histogram with corresponding colours, and the significance of the difference in the means in brackets. The errors for logarithmic parameters are in dex.

on the *NUV* magnitude. The majority of the passive spirals are not found at the extremes of the colour distribution, and lie in the green valley.

4.1 Properties of passive spirals

A comparison of average PDFs derived from the SED fitting for 19 passive and 431 normal (SSFR $> 10^{-11}$ yr^{-1}) spirals is shown in Fig. 9, and the mean values of the parameters with errors are summarized in Table C1. Physical properties of the individual passive spirals are presented in Table B1. The passive spirals have a high mean f_μ of 0.87 ± 0.02, indicating that the majority of the dust luminosity is produced in the diffuse ISM, and powered mostly by old stellar populations. The distribution of V-band optical depths in the passive and normal spirals is similar, which argues against the passive spirals being red due to higher dust obscuration. The differences found in opacity between our passive spirals and the Wolf et al. (2009) red spirals (which have twice the dust extinction of blue spirals) may be because we only examine passive spirals, and they select their sample of red spirals on the basis of optical colour alone. As we have shown in Section 3.4, red colour does not necessarily mean that galaxies are passive.

The mean M_* of the passive spirals is $(4.2^{+0.7}_{-0.6}) \times 10^{10}\,M_\odot$, in comparison to that of the normal spiral population which has a mean of $(1.9 \pm 0.1) \times 10^{10}\,M_\odot$. We find 95 per cent of the passive spirals are massive with $M_* > 10^{10}\,M_\odot$. This could be a selection bias in that we can only detect dust in the most massive passive spirals as their M_d/M_* ratios are much lower than the normal spiral population. Alternatively, Masters et al. (2010b) found that in their sample almost all red spirals were massive ($M_* > 10^{10}\,M_\odot$). Fig. 9 shows that the passive spirals in our sample have much older stellar populations than the normal spiral population. This is consistent with Masters et al. (2010b), who found red, face-on spirals have older stellar populations than blue spirals, and are not post-starburst objects. This suggests our spirals have not stopped forming stars recently, and may have low SSFR because they have used up most of their gas. This implies that, under some circumstances, spirals can retain their spiral appearance for a few Gyr following the cessation of their star formation (e.g. Bekki, Couch & Shioya 2002). This interpretation is supported by the time of last burst, for which we find a mean of $1.8^{+0.5}_{-0.4}$ Gyr for our passive spirals.

4.2 Inclination effects

Our sample of passive spirals is separated from the other morphologically classified spirals on the basis of our SED fitting results, which uses an 'angle-averaged' approach. Results may be biased for sources with high inclinations (da Cunha et al. 2010), so we calculate the inclination of our passive spirals to check that there is not a high fraction of edge-on galaxies in our sample. The minor-to-major observed axial ratio b/a of the SDSS g-band isophote at 25 mag arcsec^{-2} can be used to determine inclination. A ratio of b/a of $\sim$1 indicates that a galaxy is face-on, b/a decreases as the galaxy inclination becomes edge-on. The observed axial ratio b/a can be converted into an inclination using the relation (as used in Masters et al. 2010a)

$$\cos^2 i = \frac{(b/a)^2 - q^2}{1 - q^2}, \quad (1)$$

where q is the intrinsic axial ratio that would be measured for an edge-on galaxy ($i = 90^\circ$). An estimate of q can be obtained from the observed distribution of axial ratios for SDSS galaxies with different values of the parameter $f_{\rm Dev}$. This SDSS parameter describes the fraction of the galaxy light which is fit by a de Vaucouleurs profile (the other fraction of the luminosity is fit by an exponential profile), and gives information about the bulge-to-disc ratio. We adopt the relation found in Masters et al. (2010a) $q = 0.12 + 0.10 \times f_{\rm Dev}$, and use the g-band defined $f_{\rm Dev}$. The inclinations are listed in Table 2. Assuming that galaxies appear approximately edge-on for $i > 75^\circ$, then a random sample of inclinations would lead to 17 per cent of galaxies appearing edge-on. We find that 5/19 of our passive spirals have an edge-on inclination, and so within 2σ binomial errors our sample is consistent with a random distribution of inclinations. da Cunha et al. (2010) show that the SSFR derived from SED fitting may be biased low for high inclinations ($b/a < 0.4$, corresponding to $i > 67^\circ$). However, the SSFR of these passive spirals are sufficiently low that after accounting for this small bias we would still regard the majority of these galaxies as being passive.

We conclude that most of the 'passive' spirals are red because they harbour old stellar populations, and not because of increased amounts of dust which obscures star formation. This agrees with the findings of Masters et al. (2010b), who find that red spirals have similar dust content (measured from Balmer decrements) to blue spirals at the same stellar mass.

5 STAR FORMATION AND AGN FRACTIONS

5.1 Emission-line diagnostics

We use optical emission-line ratios plotted on a BPT diagram (Baldwin, Phillips & Terlevich 1981) to characterize the AGN activity in our H-ATLAS ETGs and spirals. Line ratios and equivalent widths (EWs) are derived from the SDSS MPA-JHU catalogue[9] (Tremonti

[9] http://www.mpa-garching.mpg.de/SDSS/DR7/

Table 2. Inclinations (i) in degrees of the 19 passive spirals in our sample. The *Herschel* SDP ID is given in Column 1, b/a is the minor-to-major observed axial ratio of the SDSS g-band isophote at 25 mag arcsec^{-2}, $f_{\rm Dev}$ is an SDSS parameter which is the fraction of the galaxy fit by a de Vaucouleurs profile and q is the intrinsic axial ratio that would be measured for $i = 90^{\circ}$.

SDP ID	b/a	$f_{\rm Dev}$	q	i
SDP.30	0.87	0.7	0.19	29.9
SDP.77	0.95	0.82	0.2	17.9
SDP.143	0.33	1.0	0.22	75.1
SDP.271	0.24	0.27	0.15	79.2
SDP.372	0.32	0.98	0.22	76.1
SDP.1544	0.78	1.0	0.22	40.0
SDP.1773	0.32	0.94	0.21	75.9
SDP.1888	0.51	0.4	0.16	60.3
SDP.2547	0.43	0.01	0.12	65.6
SDP.2612	0.31	0.0	0.12	73.1
SDP.3578	0.28	0.56	0.18	77.4
SDP.3935	0.58	0.98	0.22	56.4
SDP.4548	0.36	0.51	0.17	71.4
SDP.4639	0.73	0.02	0.12	43.9
SDP.4859	0.43	0.59	0.18	66.8
SDP.4964	0.64	0.35	0.16	51.3
SDP.5108	0.49	0.47	0.17	61.8
SDP.5226	0.62	0.95	0.22	53.4
SDP.7324	0.38	1.0	0.22	71.3

et al. 2004) and the GAMA survey (Driver et al. 2011). We regard a line detection as $>3\sigma$ above the continuum, but lines affected by sky emission or fibre fringing are not used. For line fluxes derived from the SDSS sample, corrections are made for stellar continuum absorption by subtracting a stellar population model from the spectrum, and measuring emission lines from the residual (Tremonti et al. 2004). Where line fluxes are derived from GAMA measurements, a correction of 1.3Å for stellar absorption is applied to the EW of the Hα and Hβ emission lines (Hopkins et al. 2003; Gunawardhana et al. 2011; Wijesinghe et al. 2011). Gunawardhana et al. (2011) found for Hα lines with log(Hα EW) $<$ 0.9 there was a difference of more than 5 per cent in EW when a range of absorption corrections from 0.7 to 1.3 Å was applied. Some of our sources are below log(Hα EW) $<$ 0.9, but our results are unchanged if this range of absorption corrections are used. In the cases where there are multiple measurements of the same galaxy, we take the signal-to-noise ratio weighted mean of the line fluxes.

We plot the [O III]/Hβ line ratio as a function of the [N II]/Hα, [S II]/Hα and [OI]/Hα line ratios in Fig. 10 for spirals and ETGs. We classify objects as AGN or star-forming first from the [O I]/Hα diagram, since [O I] is the most sensitive to the presence of an AGN. If the galaxy is not present in the [O I] diagram, we use the [S II]/Hα diagram, and finally the [N II]/Hα diagram. On all diagrams, galaxies that lie above the curved line are classified as AGN (Kewley et al. 2001), and galaxies below the line are star-forming. Low signal-to-noise ratio [O III] and Hβ lines mean that some sources cannot be located on the BPT diagram. In these cases, a source is classified as an AGN if [N II]/Hα $\geq$ 0.2. In many of our ETGs we do not detect all four required emission lines, so we derive upper limits and locate the galaxy on the BPT diagram where at least two lines are present.[10] We present the classification fractions of ETGs in Table 3; more than half of ETGs are star-forming, but 45 per cent of ETGs cannot be classified due to their weak emission lines. For comparison, spiral galaxies are plotted in Fig. 10 in grey, and lie mostly in the star-forming region.

In a sample of optically selected ETGs, Schawinski et al. (2007a) found 61 per cent are star-forming, and 39 per cent are AGN dominated, which is similar to the fractions in our H-ATLAS sample. Since our AGN fraction is consistent with that from an optically selected sample, this would suggest there is no link between the presence of AGN and dust emission, although it is interesting to note that we detect few LINERs[11] in our sample (although some galaxies with upper limits may fall into this category). The lack of LINERs in our sample may be because they are dust poor (Kauffmann et al. 2003b; Kewley et al. 2006), and therefore we may potentially be biased against detecting LINERS in H-ATLAS, although we need a larger sample of galaxies to confirm this.

We do not account for AGN emission in the SED fitting, so we may expect the galaxies with AGN to be poorly fit by the models. For the ETGs which host AGN, their SEDs look similar in the optical to those which are classified as star-forming. Kauffmann et al. (2003b) find that the optical spectra of type-2 AGN have a small fraction of their optical light from non-stellar sources, and are very similar to spectra of non-AGN host galaxies, except for emission lines. Since our physical properties are determined from broad-band fitting and not from line strengths, properties from optical data should not be affected by the presence of a type-2 AGN. Since Hatziminaoglou et al. (2010) find no difference between the FIR/submillimetre colours of star-forming and AGN galaxies, the FIR is insensitive to the presence of AGN and therefore will not produce a bias in SED parameters.

5.2 Hα equivalent widths

We present the Hα EW distribution of our ETGs in comparison to spirals in Fig. 11. For the ETGs there is a range in EW from 0 to 109 Å with a median of 8.7 Å, which is lower than the median for the spirals in our sample (16.4 Å). The median value for the spirals is similar to that found for field galaxies by Tresse et al. (1999). It is not unsurprising that the EW of ETGs is less than that of spirals, but none the less some EWs are substantial and indicate ongoing star formation (consistent with the broad-band SED fitting). The range of Hα EWs in ETGs are comparable to those found by Schawinski et al. (2009), who found EWs up to 85 Å in their blue ETG sample. Fukugita et al. (2004) found that visually classified ETGs (with $r <$ 15.9 and $z \lesssim 0.12$) have a similar Hα EW range as our sample, with 19 out of 420 E/S0s with Hα EW $>$ 10 Å (which represents star-forming galaxies). In our sample, we find that a much larger fraction (31 per cent) of our ETGs have Hα EW $>$ 10 Å, which is unsurprising given our submillimetre selection.

5.3 Radio detections

Another indicator of star formation and AGN activity is radio emission. Smith et al. (2011a) computed the statistical probability of

[10] In the case where there is Hβ absorption, the Hβ flux is not measured in the GAMA spectra, so we derive 3σ upper limits. Assuming a flat continuum, we estimate the area under a Gaussian line in pixels (Npix) with full width at half-maximum equal to the instrumental resolution of 3.5 Å, and estimate the error on this line given the mean noise in the spectrum (σ) as $\sqrt{\rm Npix} \times \sigma$.
[11] Low-ionization nuclear emission-line region.

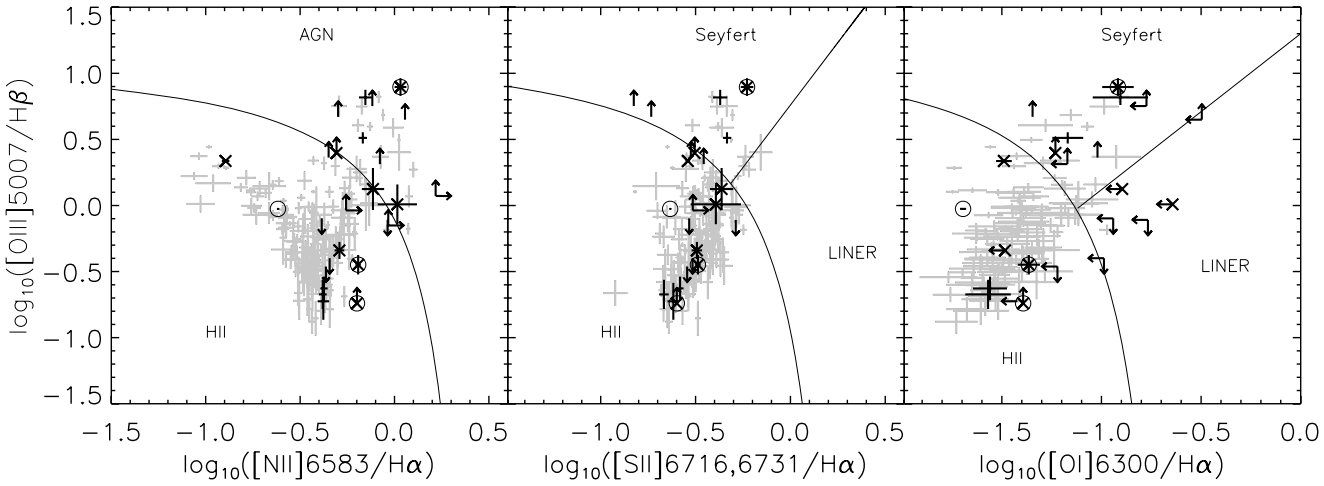

Figure 10. The BPT diagram showing H-ATLAS spirals (grey) and ETGs (black) with all four lines in each diagram detected at $>3\sigma$, with error bars shown. Those below the curved line are classified as star-forming and those above the curved line are classified as AGN. Upper limits are shown for the ETGs where at least two emission lines are detected. ETGs which have radio emission (Section 5.3) are marked with a circle, and disturbed morphologies with a diagonal cross.

Table 3. Emission-line classifications of H-ATLAS ETGs which can be unambiguously classified on the BPT diagram. These fractions do not include galaxies which we cannot classify into either category, which comprises 45 per cent of the sample. Ambiguous classifications result from one or more weak emission lines not detected at $>3\sigma$, or measurements affected by skylines. The errors are 1σ confidence intervals on a binomial population using a beta distribution, which is appropriate for small population numbers (Cameron 2011).

Classification	Number	ETG percentage
ETGs	23	100 per cent
Star-forming	13 ± 2	57^{+9}_{-10} per cent
AGN	10 ± 2	43^{+10}_{-9} per cent

a chance alignment between radio and H-ATLAS sources using the frequentist technique of Downes et al. (1986), which used a method to determine the most likely radio counterpart by choosing the source with the lowest probability P of being a chance alignment. We cross-match our ETGs with the FIRST radio catalogue and find that 5/42 ETGs have radio counterparts with $P < 0.2$, and so are considered to be likely associations. The radio emission may indicate the presence of an AGN and/or star formation, so we compute the ratio of the bolometric IR flux to the 1.4 GHz radio flux ($q_{\rm IR}$) using the method of Helou, Soifer & Rowan-Robinson (1985); Bell (2003). $q_{\rm IR}$ is defined as

$$q_{\rm IR} = \log_{10}\left(\frac{\rm TIR}{3.75\times10^{12}\,{\rm W\,m^{-2}}}\right) - \log_{10}\left(\frac{S_{1.4\,\rm GHz}}{\rm W\,m^{-2}\,Hz^{-1}}\right), \quad (2)$$

where $S_{1.4\,\rm GHz}$ is the rest-frame 1.4 GHz k-corrected flux density and TIR is the total infrared luminosity ($L_{\rm d}^{\rm tot}$), which is integrated between 3 and 1000 μm.

The $q_{\rm IR}$ values for the ETGs are presented in Table 4. Three ETGs have $q_{\rm IR}$ values consistent with that found for 162 star-forming galaxies in Bell (2003), with a median $q_{\rm IR} = 2.64 \pm 0.02$. We find two ETGs have $q_{\rm IR}$ values which are significantly lower than that for star formation, which suggests the presence of a radio-loud AGN in these galaxies. To rule out synchrotron contamination of the 500 μm flux, we extrapolate the 1.4 GHz radio flux to 500 μm using a power law with a spectral slope, α. Assuming $\alpha = -0.8$ we find that the synchrotron emission at this wavelength is negligible compared to the dust emission measured at 500 μm.

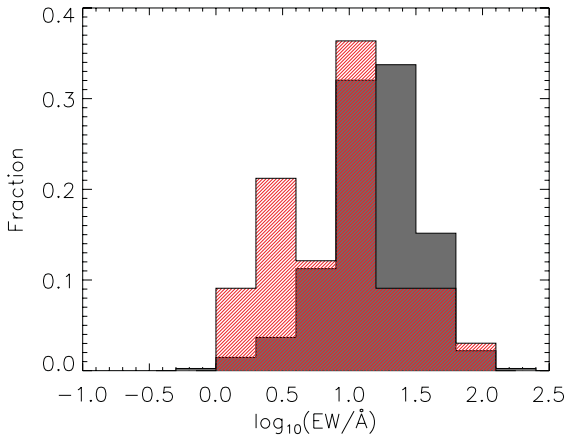

Figure 11. Hα EW (corrected for stellar absorption) of spiral galaxies (grey) and ETGs (red/hatched) which have $\geq 3\sigma$ Hα detections. A KS test shows that the ETGs have a probability of 1.7×10^{-4} of being drawn from the same distribution as the spirals.

Table 4. $q_{\rm IR}$ values for the 5/42 *Herschel* ETGs with reliable radio counterparts and SED fits. Errors are propagated from the 1σ error on TIR and the local noise estimate at the source position measured in mJy. $F_{\rm int}$ is the integrated flux density at 1.4 GHz in mJy. P is the probability of a chance alignment of the submillimetre and the radio source as computed in Smith et al. (2011a).

Name	SDP ID	P	$F_{\rm int}$	$q_{\rm IR}$
J091205.8+002656	SDP.15	0.014	4.25	2.53 ± 0.15
J090352.0−005353	SDP.45	0.048	0.98	2.59 ± 0.17
J090718.9−005210	SDP.350	0.148	1.18	2.58 ± 0.18
J090752.3+012945	SDP.1027	0.083	2.14	1.68 ± 0.41
J085947.9−002143	SDP.6427	0.077	8.62	0.86 ± 0.56

It is interesting to note that the classifications of ETGs using emission-line ratios are consistent with those from radio emission. The three ETGs with radio emission from recent star formation also have some of the bluest optical colours and largest Hα EWs, consistent with recent star formation. For the ETGs which are classified as AGN using radio emission, one (SDP.6427) is classified as an AGN using emission lines. The other (SDP.1027) is likely to be an AGN from its line emission, although it has insufficient signal-to-noise to confirm this.

5.4 Passive spirals

In most cases the spectra of the passive spirals show little or no Hα emission and a strong 4000 Å break (see Fig. B1), indicating low SFR and an old stellar population. Strong sodium and magnesium absorption is often observed in the spectra, which can indicate the presence of an old stellar population, or high metallicity. Only 4/19 passive spirals have sufficiently strong emission lines such that they can be located on a BPT diagram, and all of these are classified as AGN. This may be because AGN are more common in massive galaxies (Kauffmann et al. 2003b), although Masters et al. (2010b) found that red, face-on spirals have a higher AGN fraction than blue, face-on spirals. The lack of emission lines in the majority of the sample is consistent with their being selected as passive in terms of star formation, and also indicates a lack of AGN activity. This agrees with radio data, as there are no matches for these sources in the FIRST radio catalogue.

6 ENVIRONMENT OF HERSCHEL DETECTED SOURCES

We examine the environment of ETGs and spirals by computing the local density around each one (Brough et al., in preparation). To define the local density, we use a volume limited sample of galaxies with $M_r < -20$ and $z < 0.18$. The density Σ_N in Mpc^{-2} is computed as

$$\Sigma_N = \frac{N}{\pi d_N^2}, \tag{3}$$

where d_N is the projected comoving distance to the Nth nearest neighbour within $\pm 1000 \mathrm{kms}^{-1}$, and $N = 5$. Densities are computed for all H-ATLAS galaxies which have $r_{\mathrm{petro}} \leq 19.4$, and have good quality spectroscopic redshifts with $0.01 < z < 0.18$, which is the limit defined by the absolute magnitude limit of the sample.

6.1 H-ATLAS ETGs

Using these criteria we are able to measure densities for 30 ETGs and 354 spirals detected in H-ATLAS, which are compared in Fig. 12. The densities for ETGs and spirals both range from void to group environments (Baldry et al. 2006), with most galaxies residing in field environments. There are few H-ATLAS galaxies in group/cluster environments, so our galaxies do not sample the full range of densities in the SDP field, which range from (∼0.01 to 100) galaxies Mpc^{-2}. From the morphology–density relation (Dressler 1980), spirals are more numerous in low-density environments, and ETGs generally reside in high-density environments; however, a KS test reveals there is no significant difference between the densities of spirals and ETGs detected in H-ATLAS. This is consistent with the findings of Dariush et al. (2011), who found that the detection rate of H-ATLAS galaxies split into blue and red colours does not depend on environment. Young et al. (2011) observed a volume-limited sample of ETGs and found a statistically weak dependence

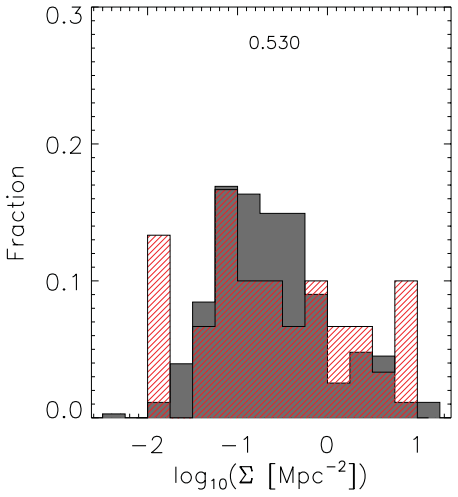

Figure 12. Comparison of densities for H-ATLAS spirals (grey) and ETGs (red/hatched). A KS test (shown at top of histogram) shows that we cannot statistically rule out the null hypothesis of the samples being drawn from the same distribution.

of molecular CO (which is often associated with star formation) on local galaxy density, where CO detections were only marginally lower in the cluster environment compared to the field. Conversely, blue ETGs have been found in lower density environments than red ETGs (Schawinski et al. 2007b; Bamford et al. 2009), although these studies sampled both field and cluster environments. Kannappan et al. (2009) found that intermediate-mass ETGs are common in low-density environments, and suggest that they may be undergoing disc re-growth.

It is possible that we are not sampling a large enough range of environments to see a significant difference in the densities of H-ATLAS sources as a function of morphology. The full H-ATLAS data set will encompass the Coma cluster and many other rich Abell clusters and will allow a more in-depth investigation of environmental effects. Since some of the H-ATLAS galaxies are in low-density regions, it is possible that our measure of environment does not always reflect the true local density, and instead traces inter-halo distances.

6.2 Passive spirals

It is thought that passive spirals have had their star formation quenched as a result of galaxy interactions with the intra-cluster medium. This can remove gas from the outer halo, which stops the supply of fuel for star formation in the disc (e.g. Bekki et al. 2002; Wolf et al. 2009). We use the local density estimates to test for any environmental differences between our passive and normal spirals, where densities can be measured for 17/19 passive spirals. Fig. 13 shows that passive spirals in our sample mostly inhabit low-density environments with a median density of 0.28 galaxies Mpc^{-2}, which is slightly higher than the median density of normal spirals (0.19 galaxies Mpc^{-2}). A KS test shows that the distributions of densities of passive and normal spirals are not significantly different, although this may be due to our small sample size. Our median density is different from Masters et al. (2010b) who found the red, face-on spiral fraction peaks at 1 Mpc^{-2}, and Bamford et al. (2009) who found that the density of red spirals peaks at 6 Mpc^{-2}. While 19 per cent of their red spirals are found at densities <1 Mpc^{-2}, we find that 71 per cent of our passive spirals lie at densities lower

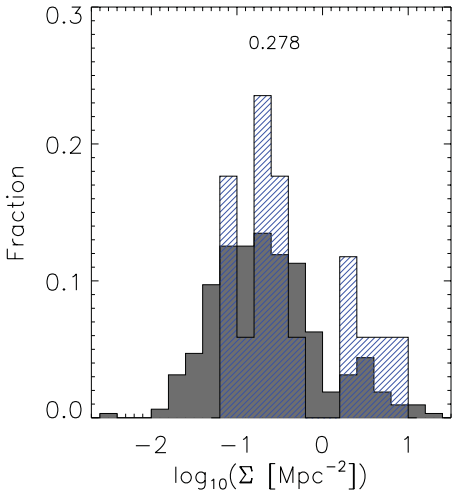

Figure 13. Environment of passive spirals with SSFR $< 10^{-11}\,\mathrm{yr}^{-1}$ detected in H-ATLAS (blue), compared to normal spirals with SSFR $> 10^{-11}\,\mathrm{yr}^{-1}$ (grey). A KS test shows a high probability (shown at the top of the histogram) that both samples are drawn from the same distribution.

than this. The differences in these fractions may be due to selection effects, since the Bamford and Masters samples are selected to be 'red', rather than 'passive', and also because our H-ATLAS spirals are in low-density environments. Our sample shows that it is possible to have passive spirals at low densities. We can conclude that environment is not the only factor influencing whether galaxies are passive, and the processes which turn spirals passive occur at both high and low densities.

7 PROPERTIES OF NON-DETECTED ETGS

We have identified a population of ETGs with substantial dust masses, some of which are actively star-forming. In order to understand how this population is different from optically selected ETGs, we compare to a control sample of morphologically classified galaxies in the SDP field which have the same $n(r, z)$ as the H-ATLAS sample, and which are not detected in H-ATLAS. The selection method for this sample is described in Section 2.1.2.

7.1 Dust masses

Our control sample comprises galaxies which are not detected in the submillimetre; however, we can investigate the average dust mass of optically selected ETGs with stacking techniques. The stacking is performed on background-subtracted, unfiltered SPIRE maps. All detected SPIRE sources are subtracted from the map, so we do not contaminate the stack. We stack at the positions of the ETGs in the control sample, using the same method as Bourne et al. (2011). We assume all galaxies are unresolved point sources, and for each source we convolve a cut-out of the map with a point spread function (PSF) centred on the optical position, which is interpolated to the same pixel grid as the data map. We share out the flux of blended sources as described in the appendix of Bourne et al. (2011), but find the effect to be negligible in this sparsely distributed sample, so double-counting of flux does not affect the stacked values. This method is effectively similar to stacking in a PSF-filtered map. The background level is estimated by stacking at random positions and this is subtracted from the stacked flux. We use the median value in the stack in order to avoid bias from outliers. Following the same method as Bourne et al. (2011), we estimate the 1σ error on the median from the distribution of values in the stack as described by Gott et al. (2001). This error estimate automatically takes into account both the measurement error, which reduces as the square root of the number of objects stacked, and the intrinsic spread of fluxes within the stack. By stacking on the positions of 233 ETGs in the control sample, we find median fluxes of 2.9 ± 0.5 mJy at 250 μm (5.8σ), 0.8 ± 0.6 mJy at 350 μm and -0.6 ± 0.6 mJy at 500 μm. The 250 μm flux is consistent with the typical fluxes of the optically red galaxies in Bourne et al. (2011).

To obtain the median stacked dust mass, we calculate the dust mass of each object in the sample from its measured flux in Jy and its redshift, using equation (4). Again the error is calculated from the distribution of dust mass values in the stack using the Gott et al. (2001) method.

$$\mathrm{M_d} = \frac{S_{250}\, D_\mathrm{L}^2 K}{\kappa_\mathrm{d}(\nu)\, B(\nu,\, T_\mathrm{d})(1+z)}. \quad (4)$$

S_{250} is the observed 250 μm flux, D_L is the luminosity distance at redshift z, $B(\nu, T_\mathrm{d})$ is the value of the Planck function at 250 μm for a dust temperature T_d, and the dust mass opacity coefficient $\kappa_\mathrm{d}(\nu)$ is $0.89\mathrm{m}^2\,\mathrm{kg}^{-1}$ (following Dunne et al. 2011). K is the k-correction, which is given by

$$K = \left(\frac{\nu_\mathrm{o}}{\nu_\mathrm{e}}\right)^{3+\beta} \frac{e^{h\nu_\mathrm{e}/kT_\mathrm{iso}} - 1}{e^{h\nu_\mathrm{o}/kT_\mathrm{iso}} - 1}, \quad (5)$$

where ν_o is the observed frequency at 250 μm, ν_e is the emitted frequency and T_iso is the isothermal temperature of a greybody model normalized to recover the stacked flux at 250 μm. We assume a dust emissivity index $\beta = 2.0$ and $T_\mathrm{iso} = 18.5$ K, which adequately describes the SEDs of optically selected galaxies (Bourne et al. 2011).

Assuming a realistic range of temperatures of 25–15 K[12] (Temi et al. 2004; Leeuw et al. 2004, M. W. L. Smith et al., in preparation), we find median dust masses ranging from $(0.8\text{–}4.0) \times 10^6\,\mathrm{M}_\odot$. The control sample dust masses of the ETGs are more than an order of magnitude smaller than the dust masses of the H-ATLAS ETGs, indicating that the 250 μm selected ETGs are indeed much dustier than the average optically selected ETG.

7.2 Star formation histories and optical colours

We use the same technique as described in Section 2.2 to fit the multiwavelength SEDs of the control sample galaxies, using 5σ upper limits for the FIR-submillimetre fluxes. We reject 27 ETGs and spirals which have poor quality SED fits with $\chi^2 > 30$. Although the parameters derived from the FIR-submillimetre region of the SED are only constrained by the UV–NIR data, we can put similar constraints on SFH parameters as for the 250 μm selected sample, as most of the constraint for SFH parameters comes from the UV–NIR photometry. A summary of the parameters derived from the mean PDFs is provided in Table C1. Stellar mass is one of the main drivers of galaxy properties, so it is important to check that the M_* distributions are the same for the H-ATLAS detected and control ETGs, so that we can compare physical properties without a dependence on galaxy mass. Fig. 14 shows the stacked PDFs of the

[12] Higher dust temperatures have been found in some studies of ETGs (e.g. Savoy et al. 2009; Skibba et al. 2011), but these used $\beta = 1.5$ which results in a higher dust temperature (∼3–4 K) being calculated (Bendo et al. 2003). Accounting for this difference in β, these studies yield dust temperatures which are consistent with our range of adopted values.

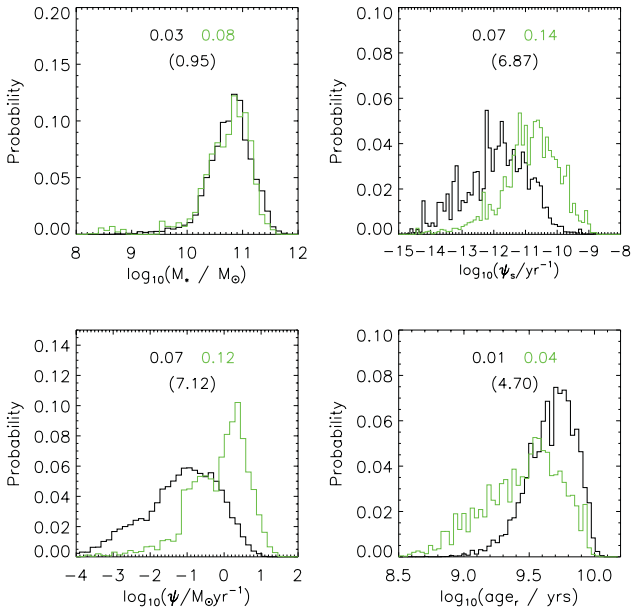

Figure 14. Average PDFs of the SED parameters of 42 detected ETGs (green line) compared to 222 control ETGs (black line). The parameters are (from left to right): M_*, stellar mass; ψ_S/yr^{-1}, SSFR; $\psi/\mathrm{M}_\odot\ \mathrm{yr}^{-1}$, SFR; and age$_r$, the r-band light-weighted age of the stellar population. The uncertainty on each distribution for ETGs and spirals is given by the error on the mean and is shown at the top of each histogram with corresponding colours, and the significance of the difference in the means in brackets. The errors for logarithmic parameters are in dex.

stellar mass distributions for H-ATLAS and control ETGs are not significantly different, since the control sample is selected to have the same r, z distribution. The range of M_d/M_* for the control ETGs is (1.4–6.8) $\times$ 10^{-5} for 25–15 K dust, and on average, the mean SSFR of the control ETGs is 1.1 dex lower than that of H-ATLAS ETGs. A similar trend is found when comparing the mean SFR of the ETGs. For our control ETGs the mean r-band light-weighted age of the stellar population is 4.6 ± 0.1 Gyr, which is 1.8 Gyr older than the H-ATLAS sample of ETGs.

The $NUV - r$ colours of the control ETGs are computed as in Section 3.4, and are compared to the H-ATLAS ETGs on a colour–magnitude diagram in Fig. 15 (a). These cover approximately the same range in M_r by design. The distribution of colours is shown in Fig. 15(b); the control ETGs are on average 1.0 mag redder than the H-ATLAS detected ETGs. Since the control ETGs are not detected in H-ATLAS these galaxies are less obscured by dust, with colours dominated by stellar population age rather than obscuration. The colour difference between detected and control ETGs is therefore intrinsic. A handful of control ETGs have very blue $NUV - r$ colours, but the dust masses of these star-forming galaxies may not be high enough to be detected by H-ATLAS. Alternatively, there could have been a failure in matching the optical counterpart and submillimetre source, which is a possibility for seven of the control ETGs (of which three are 'blue'). These, however, have a very small reliability of association as determined in Smith et al. (2011a).

7.3 Environments of *Herschel* non-detected sources

We compare the environments of control sample ETGs and spirals in Fig. 16, with densities as calculated in Section 6. As expected, on average the median density of control ETGs is higher than that of the spirals, and in contrast to the H-ATLAS ETGs and spirals,

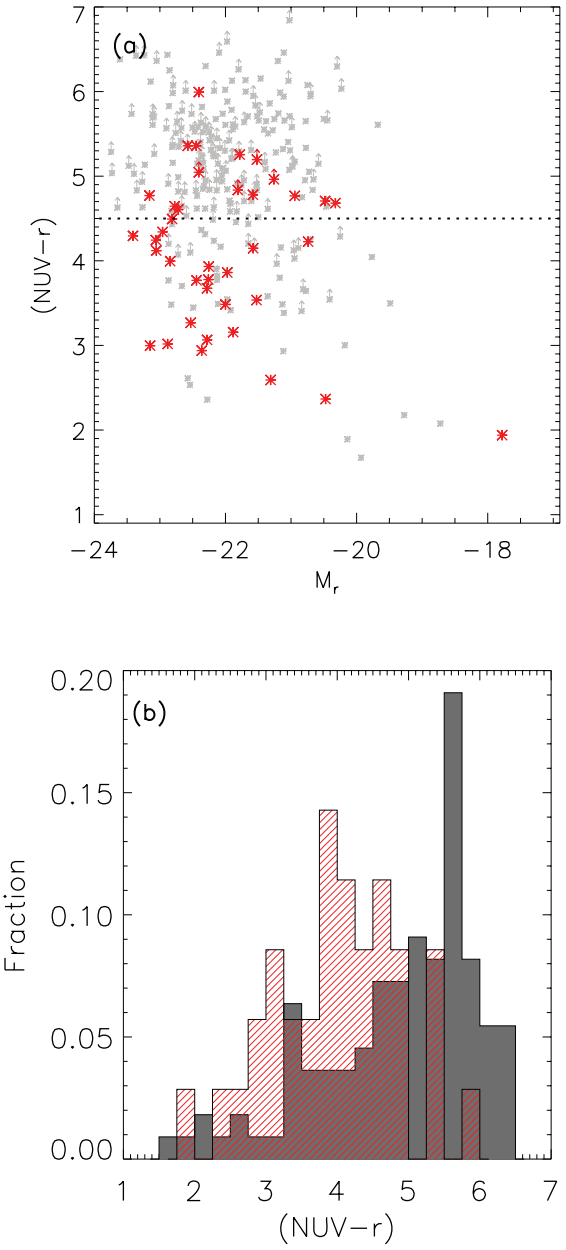

Figure 15. (a) UV-optical colour–magnitude diagram for H-ATLAS detected (red stars) and control ETGs (grey crosses). Lower limits are shown for galaxies which do not have a $\geq 5\sigma$ NUV detection. (b) Comparison of the $NUV - r$ colours for the detected ETGs (red/hatched) and control ETGs (grey/filled) which have a $\geq 5\sigma$ NUV detection.

a KS test shows a low probability of the control ETGs and spirals being drawn from the same distribution.

To see how the environments of the detected ETGs are different from those in the control sample, we compare the densities in Fig. 17(a), and find they are different at only the 1.8σ level. There is some indication that H-ATLAS ETGs are in lower density environments than optically selected ETGs, but a larger sample size is needed to confirm this. A comparison of the detected and control spirals using a KS test in Fig. 17(b) shows that we cannot statistically rule out the null hypothesis that they are drawn from the same distribution. The similarity of the distributions suggests that environment does not explain the differences between the H-ATLAS detected and control sample ETGs; however, small sample statistics

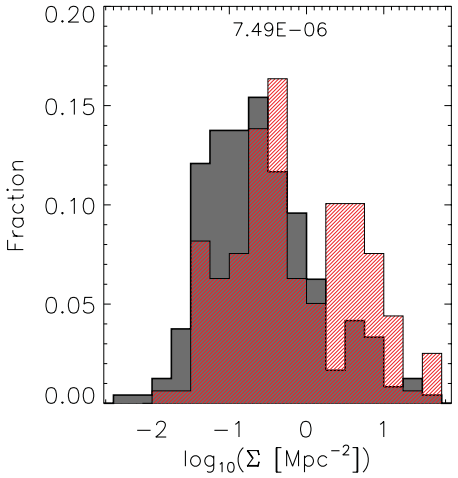

Figure 16. Comparison of densities for control sample ETGs (red/hatched) and spirals (grey). As expected, the spirals have a lower median density than the ETGs. A KS test shows a low probability of the samples of ETGs and spirals being drawn from the same distribution.

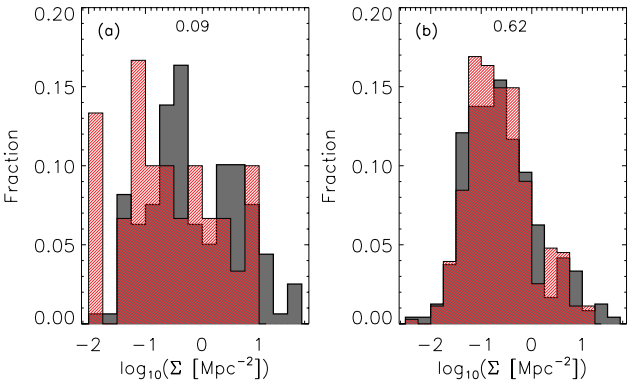

Figure 17. Comparison of environments between H-ATLAS detected (red/hatched) and control ETGs (a) and H-ATLAS and control spirals (b). For the detected and control ETGs a KS test shows the two distributions have a low probability of being drawn from the same distribution, although this is only significant at the 1.8σ level. We cannot statistically rule out the null hypothesis that the control and H-ATLAS spirals are drawn from the same distribution.

combined with a small range of environments currently limits the strength of our findings.

8 THE ORIGIN OF DUST OBSERVED IN ETGS

Interstellar dust in ETGs can originate from either an internal source (via mass-loss from stars; e.g. Goudfrooij & de Jong 1995) or an external source where gas and dust are accreted by minor mergers of galaxies or galaxy–galaxy interactions (e.g. Temi et al. 2007; Kaviraj et al. 2009; Shapiro et al. 2010). Here we use a simple approach to investigate whether stellar mass-loss could be responsible for the dust masses of the H-ATLAS ETGs.

Internal sources of interstellar dust in galaxies are poorly understood, particularly the relative contributions from supernovae (SNe) and the cool, stellar winds of low–intermediate mass stars (LIMS) in their AGB phase. In spiral galaxies like the Milky Way (MW), the major dust source is presumed to be LIMS (e.g. Whittet 2003), which inject dust at a rate of $\sim 2 \times 10^{-3}\,\mathrm{M}_{\odot}\,\mathrm{yr}^{-1}$. Dust is destroyed via sputtering in SN-driven shocks, with theoretical models predicting that dust is destroyed on time-scales of $\tau_{\mathrm{des}} \sim 300$–$800\,\mathrm{Myr}$ in the MW (Jones et al. 1994; Tielens 1998). Comparing total dust masses with destruction time-scales for both local (Jones 2001; Matsuura et al. 2009; Dunne et al. 2011) and high-redshift (Morgan & Edmunds 2003; Michałowski, Watson & Hjorth 2010; Gall, Andersen & Hjorth 2011) galaxies leads to a '*dust budget crisis*': the rates of dust injection required to maintain the observed dust mass are around an order of magnitude higher than the injection rates from LIMS.

Significant dust production in SNe would alleviate this dust budgetary problem in both local and high-z galaxies (Morgan & Edmunds 2003), yet there is still some controversy about whether SNe can produce the $\sim 1\,\mathrm{M}_{\odot}$ that would be required to alleviate the budget problem. Current estimates suggest $\sim 10^{-3}$ to $1\,\mathrm{M}_{\odot}$ of dust is formed per core-collapse SN (Rho et al. 2008; Dunne et al. 2009; Otsuka et al. 2010; Barlow et al. 2010; Matsuura et al. 2011, Krause et al., in preparation); additionally the mass of dust created (if any) in Type Ia SNe is highly uncertain.

The ISM of ETGs differs from that of spirals due to the presence of a hot X-ray emitting component at 10^6–$10^7\,\mathrm{K}$. This presents a harsh environment for dust, and indeed the destruction of dust in ETGs is thought to be dominated by thermal sputtering due to immersion in this hot gas (Jones et al. 1994), in addition to a contribution from Type 1a SNe shock collisions. For thermal sputtering in the hot ISM, the typical dust destruction time-scale is $<50\,\mathrm{Myr}$. The destruction time-scale is increased in the warm phase of the ISM ($\sim 10^4\,\mathrm{K}$) with $\tau_{\mathrm{des}} \sim 1\,\mathrm{Gyr}$ (Barlow 1978). Assuming the supernova rate in ETGs is dominated by Type Ia SNe, dust destruction due to Type Ia shocks depends on the SFR and stellar mass (e.g. Scannapieco & Bildsten 2005). Estimates for our ETGs (assuming the mean stellar mass of $4.9 \times 10^{10}\,\mathrm{M}_{\odot}$) are presented in Table 5. The time-scales for destruction from SNe shocks are much longer than those from sputtering in hot gas.

Applying all of these arguments to our sample (see Table 5 for details) the dust injection rate for an average H-ATLAS ETG would need to be 20–400 times higher than expected for LIMS and SNe. Taking the full range of derived values for the SFR for the H-ATLAS ETG sample still produces the same discrepancy. This problem is, however, not confined only to our H-ATLAS ETGs, as Dunne et al. (2011) and Gomez et al. (in preparation) found difficulty in producing enough dust in chemical evolution models for all H-ATLAS galaxies at $z < 0.5$.

The median dust mass for the control sample of ETGs is approximately 14–69 times lower than the detected sample [$M_{\mathrm{d}} = (0.8$–$4.0) \times 10^6\,\mathrm{M}_{\odot}$], with a mean SFR of $0.07\,\mathrm{M}_{\odot}\,\mathrm{yr}^{-1}$ (Table 5). If dust is destroyed only by SNe shocks then the necessary injection rate is comparable to that produced by stars; however if dust sputtering in hot gas is important then we still observe more than 10 times the amount of dust expected from stars. This suggests either sputtering is not as efficient as estimated, X-ray haloes are not as abundant or dust reforms quickly in the ISM. It is not just the control ETGs which have these issues but also the H-ATLAS ETGs.

In summary, the dust in the ETGs studied here cannot have been replenished via stellar mass-loss (see also Goudfrooij & de Jong 1995; Irwin, Stil & Bridges 2001). This result is not exclusive to ETGs since this shortfall is also seen in local and high-redshift galaxies (Morgan & Edmunds 2003) of all morphologies. Alternatively, the dust destruction time-scales in ETGs would need to be of the order of 15 Gyr (two orders of magnitude longer than currently estimated). Although this is not likely, some massive ETGs are seen without a hot X-ray ISM (Pellegrini 1999), and X-ray luminosity is found to correlate with the shape of the elliptical light profile:

Table 5. Summary of the dust sources and parameters in the H-ATLAS ETG sample with the MW and Large Magellanic Cloud shown for comparison.

	MW	LMC[a]	ETGs (H-ATLAS)	ETGs (control[b])
Average observed dust mass ($M_\odot$)	$\sim 3 \times 10^7$	2×10^6	5.5×10^7	$(0.8 - 4.0) \times 10^6$
Average SFR ($M_\odot\ yr^{-1}$)	~ 1.0	0.25	0.7	0.07
Destruction via SNe τ_{des} (Gyr)	0.5	2.5	1.2	5.0
Median dust injection rate M_d/τ_{des} ($M_\odot\ yr^{-1}$)	0.06	8×10^{-4}	0.045	$(1.6 - 8.0) \times 10^{-4}$
Range observed dust masses ($M_\odot$)	..	..	$(3.1–15.0) \times 10^7$	..
Range SFR ($M_\odot\ yr^{-1}$)	..	..	0.04-12.4	..
Range destruction via SNe τ_{des} (Gyr)	..	..	21–0.07	..
Range dust injection rate M_d/τ_{des} ($M_\odot\ yr^{-1}$)	..	..	1.5×10^{-4} to 2.2	..
Injection rate AGB stars $\dot{M}_{in,AGB}$ ($M_\odot\ yr^{-1}$)[c]	2×10^{-3}	5×10^{-5}	$(1–500) \times 10^{-4}$	1.4×10^{-4}
Injection rate SNe $\dot{M}_{in,SNe}$ ($M_\odot\ yr^{-1}$)[d]	1×10^{-3}	5×10^{-5}	$(0.5–250) \times 10^{-4}$	0.7×10^{-4}
Time to build up dust mass (Gyr)[e]	10	19	200–2	..
Time to build up average dust mass (Gyr)[e]	..	..	400–1	3.8–19.1
Contribution of dust mass from stellar sources	5 per cent	13 per cent	0.3–60 per cent	100–17 per cent
Extra dust per SNe needed ($M_\odot$)[f]	1.0	0.6–0.9	10–0.1	0.0–1.01

[a] Matsuura et al. (2009).
[b] Median dust mass of control sample for range of temperatures (15–25 K).
[c] Whittet (2003) and references therein.
[d] Rho et al. (2008) and Barlow et al. (2010) for core-collapse SNe.
[e] Calculated from $M_d/(\dot{M}_{in,AGB} + \dot{M}_{in,SNe})$ assuming no destruction.
[f] Assuming SNe are producing the dust required to match the dust injection rate.

those ETGs with power-law profiles (as opposed to cores) are generally found to have lower X-ray luminosities (Pellegrini 2005). Post-merging systems also tend to be deficient in hot gas (Read & Ponman 1998; O'Sullivan, Forbes & Ponman 2001; O'Sullivan & Ponman 2004; Brassington, Ponman & Read 2007), and a lack of X-ray emission was also found in ETGs with stellar populations <4 Gyr old (Sansom et al. 2006). Brassington et al. (2007) found that post-merger ETGs within 1 Gyr of coalescence are very underluminous in X-rays, and find tentative evidence that over the period of a few Gyr galaxies regenerate their X-ray halo. It may be the case that the dusty ETGs are examples of systems with low hot gas content, possibly seen within 1–2 Gyr after a major star formation episode which created the dust; however, X-ray observations are required to confirm this.

Longer destruction time-scales may also be achieved if a significant fraction of the star dust is shielded from the hot gas in a cool, dense phase of the ISM. Recent observations of ETGs have detected significant amounts of cold CO gas (Young et al. 2011), with a detection rate of 22 per cent in a volume-limited sample of ETGs. It is possible that since our ETGs have significant dust mass they also have a large cold gas content; however observations of molecular gas are required to test this hypothesis.

Finally, multiple lines of evidence now favour dust growth in the cold neutral phase ($n_H > 30\,cm^{-3}$) of the ISM on rapid time-scales of $\sim$Myr (Draine & Salpeter 1979; Dwek & Scalo 1980; Tielens 1998; Draine 2009). Such growth can replenish dust mass lost through shocks and thermal sputtering (although seed nuclei must survive sputtering in order for this to occur). Given the shortfall of dust from stars, one would then conclude that most (i.e. 40–99 per cent; Table 5) of the dust in the ISM of *Herschel* detected ETGs would need to be grown *in* the ISM. The dust yield of a galaxy would depend only on balancing destruction time-scales with the formation conditions in the ISM.

The other scenario we can consider is that mergers with dust-rich galaxies could account for the dust content of the *Herschel* ETGs. Such a case was demonstrated recently when Gomez et al. (2010) detected $\sim 10^6\,M_\odot$ of dust associated with M86 which originated from a recent tidal interaction with the nearby spiral NGC 4438; this is of the same order as the dust mass in the stacked, un-detected sample. However, to explain the discrepancy between the observed total dust mass in the *Herschel*-detected ETGs and the dust mass provided via stellar mass-loss, we would require $>10^7\,M_\odot$ of dust to be accreted. This is akin to the average ETG in this sample swallowing a large spiral galaxy with an equivalent dust mass to the MW in its recent history. As indicated by Maller et al. (2006), the major merger rate at $z = 0.3$ is $0.018\,Gyr^{-1}$ ($M_{gal} < 6.4 \times 10^{10}\,M_\odot$) to $0.054\,Gyr^{-1}$ ($M_{gal} > 6.4 \times 10^{10}\,M_\odot$) per galaxy. The small fraction of dusty ETGs (5.5 per cent) relative to similar optically selected ETGs could be produced assuming that the dusty ETGs are being observed within 0.5–1 Gyr after major morphological disturbance has subsided (Lotz et al. 2008), on the assumption that sputtering does not destroy the dust grains. Observations of gas and stellar kinematics are required to test this hypothesis. Lower levels of dust in other ETG samples are thought to be due to minor mergers (e.g. Temi et al. 2007), although in the case of our sample this is less plausible since the rate of such mergers needs to be very high to create and sustain the dust mass.

Since only a small fraction of ETGs have dust masses as large as those detected in *Herschel*-ATLAS, it could be that our sample represents a short-lived phase in the evolution of some ETGs. Either we are seeing ETGs at a time when dust is present following a major merger, and the hot X-ray component is also suppressed in this phase, allowing the dust to survive. Alternatively, we have a sample of ETGs with sufficient residual ISM left over from star formation to provide a haven for the dust grains to grow and survive the hot X-ray gas (which may also be less abundant than average in these galaxies). Current dust destruction time-scales are inconsistent with the amount of dust observed in both H-ATLAS and control ETGs. We can only account for the dust observed in some H-ATLAS ETGs if we assume maximal supernova dust production (in Type I and II SNe), and no destruction, which would produce $\sim 1 \times 10^7\,M_\odot$ of dust in 1 Gyr.

Further observations to study the kinematics, light profiles, gas content and X-ray properties of this sample will be required to fully

answer the question of the origin of this dust. A more detailed investigation of the evolution of dust in these galaxies using a detailed chemical evolution model will be presented in Gomez et al. (in preparation).

9 CONCLUSIONS

We present the properties of a 250 μm selected sample of galaxies according to their morphology. Our sample consists of 44 ETGs and 496 spiral galaxies in the 14 deg^2 SDP field. Using an energy balance method of SED fitting we derive physical parameters, and use these to compare the properties of H-ATLAS galaxies as a function of morphological type. We also compare to a control sample of optical galaxies selected to have the same $n(r, z)$ as the H-ATLAS sample. Our main results are as follows.

(i) ETGs detected by *Herschel* are atypical compared to optically selected ETGs. We detect significant dust masses in H-ATLAS ETGs, with a mean of 5.5×10^7 M$_\odot$. Through stacking we find that dust masses are an order of magnitude lower in optically selected ETGs of a similar stellar mass.

(ii) Only a small fraction of H-ATLAS ETGs (24 per cent) have evidence for a recent burst of star formation within the past Gyr. Some of these galaxies may have had star formation triggered as a result of an interaction, indicated by disturbed morphologies in 31 per cent of the sample, although not all disturbed sources show signs of a recent burst. The majority have residual low-level star formation left over from the last burst a few Gyr ago, and their optical colours suggest they exist in the transition region between the blue cloud and the red sequence.

(iii) We find that the control ETGs have lower SSFRs and older stellar population ages than H-ATLAS ETGs, which is consistent with the red UV-optical colours of the control ETGs. It is possible that the dust content may therefore be related to the time of the last major star formation episode several Gyr ago.

(iv) No significant difference is found in the environments of H-ATLAS and control ETGs, although this may be due to small sample size. Environment does not seem to influence whether an ETG is dusty, at the moderate–low densities probed in this study. Additionally, we do not find any H-ATLAS ETGs in high-density environments.

(v) The 5.5 per cent of ETGs detected in H-ATLAS (compared to an optical sample of similar stellar mass) contain more dust than can be accounted for by production in AGB stars, although this problem also extends to the control ETGs (except at the very lowest median dust mass). Most of the dust must be formed in the ISM, or an external source of dust from major mergers is also a possibility. It is also possible that in H-ATLAS and control ETGs the dust destruction time-scale is longer if they are deficient in X-ray gas. Future studies of the kinematics of the gas and stars would be beneficial in testing this hypothesis, in addition to X-ray and CO observations.

(vi) We examine the properties of passive spirals in our sample which have low SSFR $< 10^{-11}$ yr^{-1}, but still contain significant dust mass. They have larger M_* and lower $M_{\rm d}/M_*$ than 'normal' spirals, and are red in colour, which is due to an old stellar population, and not due to increased dust reddening. It is possible that these passive spirals have simply run out of gas to fuel star formation, or their star formation has been quenched by some process in the low-density environment in which they reside.

Using *Herschel* we can probe the dust content of different types of galaxies over a wide range of redshifts. The full coverage of the H-ATLAS survey will allow more investigation, with far larger numbers of ETGs and passive spirals. This will improve our understanding of objects which are transitioning between the blue and red sequence, either through rejuvenated star formation or through the cessation of star formation as the supply of gas ends.

ACKNOWLEDGMENTS

We would like to thank the anonymous referee for important suggestions which helped us improve the paper. We also thank Luca Cortese, Alfonso Aragón-Salamanca and Andrew Baker for their helpful comments. The Herschel-ATLAS is a project with *Herschel*, which is an ESA space observatory with science instruments provided by European-led Principal Investigator consortia and with important participation from NASA. The H-ATLAS website is http://www.h-atlas.org/.

GAMA is a joint European-Australasian project based around a spectroscopic campaign using the Anglo-Australian Telescope. The GAMA input catalogue is based on data taken from the SDSS and the UKIRT Infrared Deep Sky Survey. Complementary imaging of the GAMA regions is being obtained by a number of independent survey programmes including *GALEX* MIS, VST KIDS, VISTA VIKING, *WISE*, *Herschel*-ATLAS, GMRT and ASKAP providing UV-to-radio coverage. GAMA is funded by the STFC (UK), the ARC (Australia), the AAO and the participating institutions. The GAMA website is http://www.gama-survey.org/. The Italian group acknowledges partial financial support from ASI/INAF agreement n. I/009/10/0.

REFERENCES

Abazajian K. N. et al., 2009, ApJS, 182, 543
Adelman-McCarthy J. K. et al., 2008, ApJS, 175, 297
Baldry I. K., Glazebrook K., Brinkmann J., Ivezić Ž., Lupton R. H., Nichol R. C., Szalay A. S., 2004, ApJ, 600, 681
Baldry I. K., Balogh M. L., Bower R. G., Glazebrook K., Nichol R. C., Bamford S. P., Budavari T., 2006, MNRAS, 373, 469
Baldry I. K. et al., 2010, MNRAS, 404, 86
Baldwin J. A., Phillips M. M., Terlevich R., 1981, PASP, 93, 5
Bamford S. P. et al., 2009, MNRAS, 393, 1324
Barlow M. J., 1978, MNRAS, 183, 367
Barlow M. J. et al., 2010, A&A, 518, L138
Becker R. H., White R. L., Helfand D. J., 1995, ApJ, 450, 559
Bekki K., Couch W. J., Shioya Y., 2002, ApJ, 577, 651
Bell E. F., 2003, ApJ, 586, 794
Bell E. F. et al., 2004, ApJ, 608, 752
Bendo G. J. et al., 2003, AJ, 125, 2361
Blanton M. R., Roweis S., 2007, AJ, 133, 734
Blanton M. R. et al., 2003, ApJ, 594, 186
Bourne N. et al., 2011, MNRAS, submitted
Brassington N. J., Ponman T. J., Read A. M., 2007, MNRAS, 377, 1439
Bregman J. N., Snider B. A., Grego L., Cox C. V., 1998, ApJ, 499, 670
Bruzual G., Charlot S., 2003, MNRAS, 344, 1000
Cameron E., 2011, Proc. Astron. Soc. Australia, 28, 128
Chabrier G., 2003, PASP, 115, 763
Charlot S., Fall S. M., 2000, ApJ, 539, 718
Cimatti A. et al., 2004, Nat, 430, 184
Colless M. et al., 2001, MNRAS, 328, 1039
Cortese L., Hughes T. M., 2009, MNRAS, 400, 1225
Cortese L. et al., 2010, A&A, 518, L63
da Cunha E., Charlot S., Elbaz D., 2008, MNRAS, 388, 1595 (DCE08)
da Cunha E., Eminian C., Charlot S., Blaizot J., 2010, MNRAS, 403, 1894
Dariush A. et al., 2011, MNRAS, 418, 64
De Propris R., Conselice C. J., Liske J., Driver S. P., Patton D. R., Graham A. W., Allen P. D., 2007, ApJ, 666, 212
De Propris R. et al., 2010, AJ, 139, 794

de Zeeuw P. T. et al., 2002, MNRAS, 329, 513
Downes A. J. B., Peacock J. A., Savage A., Carrie D. R., 1986, MNRAS, 218, 31
Draine B. T., 2009, in Henning T., Grün E., Steinacker J., eds, ASP Conf. Ser. Vol. 414. Cosmic Dust – Near and Far. Interstellar Dust Models and Evolutionary Implications. Astron. Soc. Pac., San Francisco, p. 453
Draine B. T., Salpeter E. E., 1979, ApJ, 231, 438
Dressler A., 1980, ApJ, 236, 351
Driver S. P. et al., 2006, MNRAS, 368, 414
Driver S. P. et al., 2011, MNRAS, 413, 971
Dunne L., Eales S. A., 2001, MNRAS, 327, 697
Dunne L. et al., 2009, MNRAS, 394, 1307
Dunne L. et al., 2011, MNRAS, 417, 1510
Dwek E., Scalo J. M., 1980, ApJ, 239, 193
Eales S. et al., 2010, PASP, 122, 499
Faber S. M. et al., 2007, ApJ, 665, 265
Fukugita M., Nakamura O., Turner E. L., Helmboldt J., Nichol R. C., 2004, ApJ, 601, L127
Gall C., Andersen A. C., Hjorth J., 2011, A&A, 528, A13
Gehrels N., 1986, ApJ, 303, 336
Gomez H. L. et al., 2010, A&A, 518, L45
Goto T., Yamauchi C., Fujita Y., Okamura S., Sekiguchi M., Smail I., Bernardi M., Gomez P. L., 2003, MNRAS, 346, 601
Gott J. R., III, Vogeley M. S., Podariu S., Ratra B., 2001, ApJ, 549, 1
Goudfrooij P., de Jong T., 1995, A&A, 298, 784
Griffin M. J. et al., 2010, A&A, 518, L3
Gunawardhana M. L. P. et al., 2011, MNRAS, 415, 1647
Hatziminaoglou E. et al., 2010, A&A, 518, L33
Hawarden T. G., Longmore A. J., Tritton S. B., Elson R. A. W., Corwin H. G., Jr,, 1981, MNRAS, 196, 747
Helou G., Soifer B. T., Rowan-Robinson M., 1985, ApJ, 298, L7
Hill D. T. et al., 2011, MNRAS, 412, 765
Hopkins A. M. et al., 2003, ApJ, 599, 971
Hughes T. M., Cortese L., 2009, MNRAS, 396, L41
Ibar E. et al., 2010, MNRAS, 409, 38
Irwin J. A., Stil J. M., Bridges T. J., 2001, MNRAS, 328, 359
Jones A. P., 2001, R. Soc. Lond. Philos. Trans. Series A, 359, 1961
Jones A. P., Tielens A. G. G. M., Hollenbach D. J., McKee C. F., 1994, ApJ, 433, 797
Kannappan S. J., Guie J. M., Baker A. J., 2009, AJ, 138, 579
Kauffmann G. et al., 2003a, MNRAS, 341, 54
Kauffmann G. et al., 2003b, MNRAS, 346, 1055
Kaviraj S., 2010, MNRAS, 406, 382
Kaviraj S. et al., 2007, ApJS, 173, 619
Kaviraj S. et al., 2008, MNRAS, 388, 67
Kaviraj S., Peirani S., Khochfar S., Silk J., Kay S., 2009, MNRAS, 394, 1713
Kaviraj S., Tan K., Ellis R. S., Silk J., 2011a, MNRAS, 411, 2148
Kaviraj S. et al., 2011b, preprint (arXiv:1107.5306)
Kennicutt R. C., Jr, 1998, ApJ, 498, 541
Kewley L. J., Heisler C. A., Dopita M. A., Lumsden S., 2001, ApJS, 132, 37
Kewley L. J., Groves B., Kauffmann G., Heckman T., 2006, MNRAS, 372, 961
Lawrence A. et al., 2007, MNRAS, 379, 1599
Leeuw L. L., Sansom A. E., Robson E. I., Haas M., Kuno N., 2004, ApJ, 612, 837
Leeuw L. L., Davidson J., Dowell C. D., Matthews H. E., 2008, ApJ, 677, 249
Lintott C. J. et al., 2008, MNRAS, 389, 1179
Lintott C. et al., 2011, MNRAS, 410, 166
Lotz J. M. et al., 2008, ApJ, 672, 177
Maller A. H., Katz N., Kereš D., Davé R., Weinberg D. H., 2006, ApJ, 647, 763
Martin D. C. et al., 2005, ApJ, 619, L1
Masters K. L. et al., 2010a, MNRAS, 404, 792
Masters K. L. et al., 2010b, MNRAS, 405, 783
Matsuura M. et al., 2009, MNRAS, 396, 918
Matsuura M. et al., 2011, Sci, 333, 1258
Michałowski M. J., Watson D., Hjorth J., 2010, ApJ, 712, 942
Morgan H. L., Edmunds M. G., 2003, MNRAS, 343, 427
Morrissey P. et al., 2007, ApJS, 173, 682
Moshir M., Kopman G., Conrow T. A. O., 1992, *IRAS* Faint Source Survey, Explanatory Supplement Version 2. JPL, Pasadena
Negrello M. et al., 2010, Sci, 330, 800
O'Connell R. W., 1999, ARA&A, 37, 603
O'Sullivan E., Ponman T. J., 2004, MNRAS, 349, 535
O'Sullivan E., Forbes D. A., Ponman T. J., 2001, MNRAS, 324, 420
Otsuka M. et al., 2010, A&A, 518, L139
Pascale E. O., 2011, MNRAS, 415, 911
Pellegrini S., 1999, A&A, 351, 487
Pellegrini S., 2005, ApJ, 624, 155
Pilbratt G. L. et al., 2010, A&A, 518, L1
Poggianti B. M., Smail I., Dressler A., Couch W. J., Barger A. J., Butcher H., Ellis R. S., Oemler A., Jr, 1999, ApJ, 518, 576
Poggianti B. M., Bridges T. J., Komiyama Y., Yagi M., Carter D., Mobasher B., Okamura S., Kashikawa N., 2004, ApJ, 601, 197
Poglitsch A. et al., 2010, A&A, 518, L2
Read A. M., Ponman T. J., 1998, MNRAS, 297, 143
Rho J. et al., 2008, ApJ, 673, 271
Rigby E. E. et al., 2011, MNRAS, 415, 2336
Robotham A. et al., 2010, Proc. Astr. Soc. Australia, 27, 76
Sadler E. M., Gerhard O. E., 1985, MNRAS, 214, 177
Sansom A. E., O'Sullivan E., Forbes D. A., Proctor R. N., Davis D. S., 2006, MNRAS, 370, 1541
Savoy J., Welch G. A., Fich M., 2009, ApJ, 706, 21
Scannapieco E., Bildsten L., 2005, ApJ, 629, L85
Schawinski K., Thomas D., Sarzi M., Maraston C., Kaviraj S., Joo S., Yi S. K., Silk J., 2007a, MNRAS, 382, 1415
Schawinski K. et al., 2007b, ApJS, 173, 512
Schawinski K. et al., 2009, MNRAS, 396, 818
Schlegel D. J., Finkbeiner D. P., Davis M., 1998, ApJ, 500, 525
Shapiro K. L. et al., 2010, MNRAS, 402, 2140
Skibba R. A. et al., 2009, MNRAS, 399, 966
Skibba R. A. et al., 2011, ApJ, 738, 89
Smith D. J. B. et al., 2011a, MNRAS, 416, 857
Smith D. J. B. et al., 2011b, MNRAS, submitted
Stickel M., Klaas U., Lemke D., 2007, A&A, 466, 831
Strateva I. et al., 2001, AJ, 122, 1861
Sutherland W., Saunders W., 1992, MNRAS, 259, 413
Temi P., Brighenti F., Mathews W. G., Bregman J. D., 2004, ApJS, 151, 237
Temi P., Brighenti F., Mathews W. G., 2007, ApJ, 660, 1215
Temi P., Brighenti F., Mathews W. G., 2009a, ApJ, 695, 1
Temi P., Brighenti F., Mathews W. G., 2009b, ApJ, 707, 890
Thomas D., Maraston C., Bender R., Mendes de Oliveira C., 2005, ApJ, 621, 673
Tielens A. G. G. M., 1998, ApJ, 499, 267
Tremonti C. A. et al., 2004, ApJ, 613, 898
Tresse L., Maddox S., Loveday J., Singleton C., 1999, MNRAS, 310, 262
van den Bergh S., 1976, ApJ, 206, 883
van Dokkum P. G., Franx M., 1995, AJ, 110, 2027
Vlahakis C., Dunne L., Eales S., 2005, MNRAS, 364, 1253
Walcher C. J. et al., 2008, A&A, 491, 713
Wei L. H., Kannappan S. J., Vogel S. N., Baker A. J., 2010, ApJ, 708, 841
Whittet D. C. B., ed., 2003, Dust in the Galactic Environment. IoP Publishing, Bristol
Wijesinghe D. B. et al., 2011, MNRAS, 410, 2291
Wild V., Walcher C. J., Johansson P. H., Tresse L., Charlot S., Pollo A., Le Fèvre O., de Ravel L., 2009, MNRAS, 395, 144
Wolf C., Gray M. E., Meisenheimer K., 2005, A&A, 443, 435
Wolf C. et al., 2009, MNRAS, 393, 1302
Yi S., Demarque P., Oemler A., Jr, 1997, ApJ, 486, 201
Yi S. K. et al., 2005, ApJ, 619, L111
Young L. M. et al., 2011, MNRAS, 414, 940

APPENDIX A: EARLY-TYPE GALAXIES

Table A1. Properties of ETGs derived from SED fitting. The columns are (from left to right): ID, SDP ID, redshift, SDSS RA, SDSS Dec., 250 μm flux in Jy, f_μ, the fraction of total dust luminosity contributed by the diffuse ISM; $\hat{\tau}_V$, total effective V-band optical depth seen by stars in birth clouds; $M_*/M_\odot$, log(stellar mass); $L_d^{tot}/L_\odot$, log(dust luminosity); T_C^{ISM}/K, temperature of the cold ISM dust component; $\hat{\tau}_V^{ISM}$, the V-band optical depth in the ambient ISM. $M_d/M_\odot$, log(dust mass); ψ_S/yr^{-1}, log(SSFR); $\psi/M_\odot yr{-}1$, log(SFR), t_{LB}, log(time of last burst); age$_r$, log(r-band light-weighted age of the stellar population), rest-frame $NUV - r$ colour (Section 3.4), density (Σ/galaxies Mpc^{-2}, see Section 6) Hα EW/Å (corrected for stellar absorption of 1.3 Å if $>3\sigma$ detection). An asterisk (*) indicates morphological disturbance.

ID	SDP ID	z	RA	Dec.	F_{250}	f_μ	$\hat{\tau}_V$	M_*	L_d^{tot}	T_C^{ISM}	$\hat{\tau}_V^{ISM}$	M_d	ψ_S	ψ	t_{LB}	age$_r$	$NUV - r$	Σ	Hα EW
J091205.8+002656	15*	0.05	138.024	0.449	0.38	0.50	3.60	10.20	11.00	24.1	1.27	7.58	−9.47	0.74	9.04	9.08	–	2.92	27.54
J091448.7−003533	35*	0.05	138.704	−0.592	0.25	0.73	2.31	10.45	10.44	21.5	0.69	7.50	−10.40	0.07	9.38	9.52	–	1.02	8.39
J090352.0−005353	45*	0.10	135.967	−0.898	0.20	0.73	2.20	10.96	11.00	22.2	0.64	7.97	−10.34	0.62	9.25	9.41	3.77	0.06	14.87
J091051.1+020121	128	0.05	137.714	2.022	0.11	0.58	1.71	9.87	10.00	15.7	0.46	7.74	−10.06	−0.13	9.05	9.29	2.59	0.46	12.63
J090234.3+012518	159	0.12	135.643	1.421	0.11	0.93	3.02	10.96	10.72	22.9	0.88	7.75	−11.39	−0.44	9.31	9.67	5.25	1.08	5.24
J090647.7+011555	186	0.15	136.699	1.265	0.10	0.57	2.53	10.50	10.91	20.4	0.48	8.03	−9.72	0.79	8.69	9.00	3.07	0.08	24.35
J090101.2−005541	273	0.09	135.256	−0.929	0.09	0.68	1.10	10.82	10.36	19.0	0.21	7.67	−10.71	0.12	9.33	9.51	3.93	0.01	5.01
J090238.7+013253	311	0.12	135.661	1.548	0.09	0.68	2.44	10.38	10.78	23.0	0.82	7.67	−9.97	0.46	8.61	9.11	3.54	0.63	39.30
J090223.1+010709	328*	0.20	135.597	1.120	0.09	0.83	2.08	11.02	11.04	20.8	0.60	8.22	−10.63	0.44	8.90	9.31	4.34	–	8.87
J090718.9−005210	350	0.06	136.829	−0.869	0.09	0.36	1.33	9.65	10.55	24.1	0.50	6.93	−9.25	0.41	8.80	8.92	2.37	0.01	109.07
J091332.4+000631	366*	0.23	138.386	0.108	0.08	0.93	3.65	10.88	11.13	23.7	0.84	8.07	−10.96	−0.09	8.78	9.00	4.49	–	14.76
J091023.1+014023	370	0.14	137.596	1.673	0.08	0.95	3.68	10.82	10.46	15.7	0.71	8.40	−11.88	−1.08	9.48	9.80	>5.19	0.07	0.48
J090952.3−003019	451	0.05	137.468	−0.505	0.09	0.90	1.86	10.28	9.93	22.4	0.56	6.97	−11.17	−0.93	9.35	9.65	4.68	0.01	12.69
J085915.7+002329	457*	0.01	134.815	0.392	0.09	0.30	0.67	8.62	8.76	18.3	0.14	5.97	−9.51	−1.00	9.16	9.28	1.94	–	45.87
J090551.5+010752	628*	0.05	136.465	1.131	0.07	0.92	1.08	11.18	9.94	21.7	0.12	6.98	−12.27	−1.10	9.57	9.92	5.99	0.17	1.70
J090522.1−005925	786	0.10	136.343	−0.991	0.08	0.80	1.58	10.91	10.40	20.3	0.26	7.57	−11.04	−0.12	9.41	9.60	–	0.08	1.59
J090752.3+012945	1027	0.10	136.968	1.496	0.07	0.80	1.28	11.06	10.36	20.3	0.20	7.58	−11.16	−0.09	9.52	9.67	4.61	3.24	1.39
J085852.1+010624	1278	0.12	134.718	1.106	0.06	0.63	1.14	10.60	10.35	17.4	0.20	7.87	−10.47	0.18	8.86	9.24	3.67	0.50	2.21
J091037.8+015654	1372*	0.23	137.658	1.949	0.06	0.55	2.41	10.76	10.99	19.4	0.37	8.20	−9.88	0.88	8.77	9.05	3.02	–	32.32
J090929.3+020327	1409	0.15	137.373	2.057	0.06	0.92	1.85	11.17	10.49	19.4	0.31	7.86	−11.70	−0.49	9.36	9.67	5.36	0.26	1.30
J090618.0−002455	1955*	0.17	136.575	−0.415	0.05	0.66	2.30	10.92	10.68	20.1	0.38	7.85	−10.53	0.40	9.40	9.51	3.78	0.28	3.49
J090259.5+020046	2025	0.07	135.747	2.012	0.05	0.85	2.12	10.34	9.87	18.5	0.45	7.36	−11.14	−0.79	9.53	9.74	4.71	0.08	8.11
J085934.1+003629	2311*	0.26	134.892	0.608	0.05	0.90	2.02	11.20	10.81	16.3	0.47	8.64	−11.20	−0.01	9.27	9.61	4.64	–	2.47
J085842.0+010956	2364	0.12	134.677	1.166	0.06	0.86	1.49	10.96	10.42	19.5	0.36	7.73	−11.18	−0.25	9.31	9.58	4.12	0.67	3.55
J085944.2+011708	2702	0.16	134.933	1.285	0.05	0.94	2.18	10.88	10.43	17.2	0.52	8.11	−11.73	−0.86	9.37	9.66	>4.84	0.59	1.78
J090634.8+020752	2853	0.25	136.645	2.132	0.04	0.82	1.14	11.39	10.88	19.0	0.31	8.25	−11.05	0.32	9.46	9.59	4.29	–	2.37
J090210.6+004805	2945	0.20	135.545	0.802	0.05	0.46	1.51	10.70	10.88	18.3	0.32	8.10	−9.89	0.80	9.46	9.27	2.94	–	9.97
J085727.4+010847	2959	0.07	134.364	1.146	0.05	0.78	1.51	10.30	9.84	20.1	0.31	7.09	−10.90	−0.66	9.48	9.63	4.23	2.80	5.19
J091359.4+000909	3005	0.17	138.498	0.152	0.04	0.92	1.95	10.58	10.41	17.5	0.55	8.05	−11.17	−0.55	8.91	9.38	4.78	6.02	1.30
J090236.7+011909	3252	0.09	135.653	1.320	0.06	0.95	1.58	11.03	10.14	19.7	0.19	7.49	−12.37	−1.37	9.47	9.77	5.36	0.17	0.38
J090849.5−001846	3321	0.22	137.208	−0.313	0.04	0.72	1.62	11.07	10.76	19.1	0.32	8.08	−10.65	0.40	9.39	9.50	4.00	–	2.46
J091435.2−003919	3549	0.32	138.648	−0.655	0.04	0.54	1.72	11.19	11.24	21.5	0.43	8.17	−10.09	1.09	9.41	9.36	3.00	–	6.21
J091409.6+000439	3702	0.16	138.541	0.078	0.04	0.74	2.20	10.69	10.49	17.4	0.51	8.06	−10.55	0.11	9.15	9.45	4.15	6.99	3.99
J090938.9−005753	3834	0.13	137.412	−0.966	0.04	0.94	2.16	10.56	10.22	18.8	0.50	7.67	−11.68	−1.10	9.10	9.48	>4.96	0.04	–
J091315.8+004445	5088	0.23	138.315	0.746	0.04	0.71	1.56	11.05	10.68	16.9	0.22	8.31	−10.69	0.38	8.95	9.30	4.24	–	19.50
J090936.0+023324	5311	0.16	137.399	2.557	0.04	0.66	1.38	10.58	10.48	19.9	0.31	7.67	−10.35	0.19	9.28	9.41	3.48	7.44	15.18
J091054.2+005454	5382	0.16	137.726	0.916	0.04	0.69	1.68	10.80	10.48	17.6	0.33	7.95	−10.65	0.14	9.48	9.55	3.86	0.22	3.55
J091143.5+012053	5489	0.07	137.932	1.349	0.04	0.82	1.81	10.49	9.83	20.9	0.26	6.98	−11.20	−0.70	9.38	9.62	4.77	0.04	2.70
J090310.3+014233	6310	0.16	135.793	1.709	0.04	0.57	1.71	10.57	10.48	17.3	0.28	7.93	−10.25	0.31	9.45	9.47	3.16	0.11	8.74
J085916.4+005218	6337	0.24	134.819	0.873	0.04	0.59	1.68	10.66	10.80	18.6	0.32	8.10	−10.05	0.63	8.78	9.09	3.27	–	8.75
J085947.9−002143	6427*	0.12	134.95	−0.363	0.05	0.87	1.65	11.00	10.16	21.2	0.18	7.34	−11.54	−0.56	9.47	9.65	4.77	0.01	12.04
J090413.9−004405	6640*	0.20	136.058	−0.734	0.04	0.94	1.97	11.10	10.52	20.0	0.37	7.82	−12.03	−0.90	9.33	9.63	>5.05	–	2.60

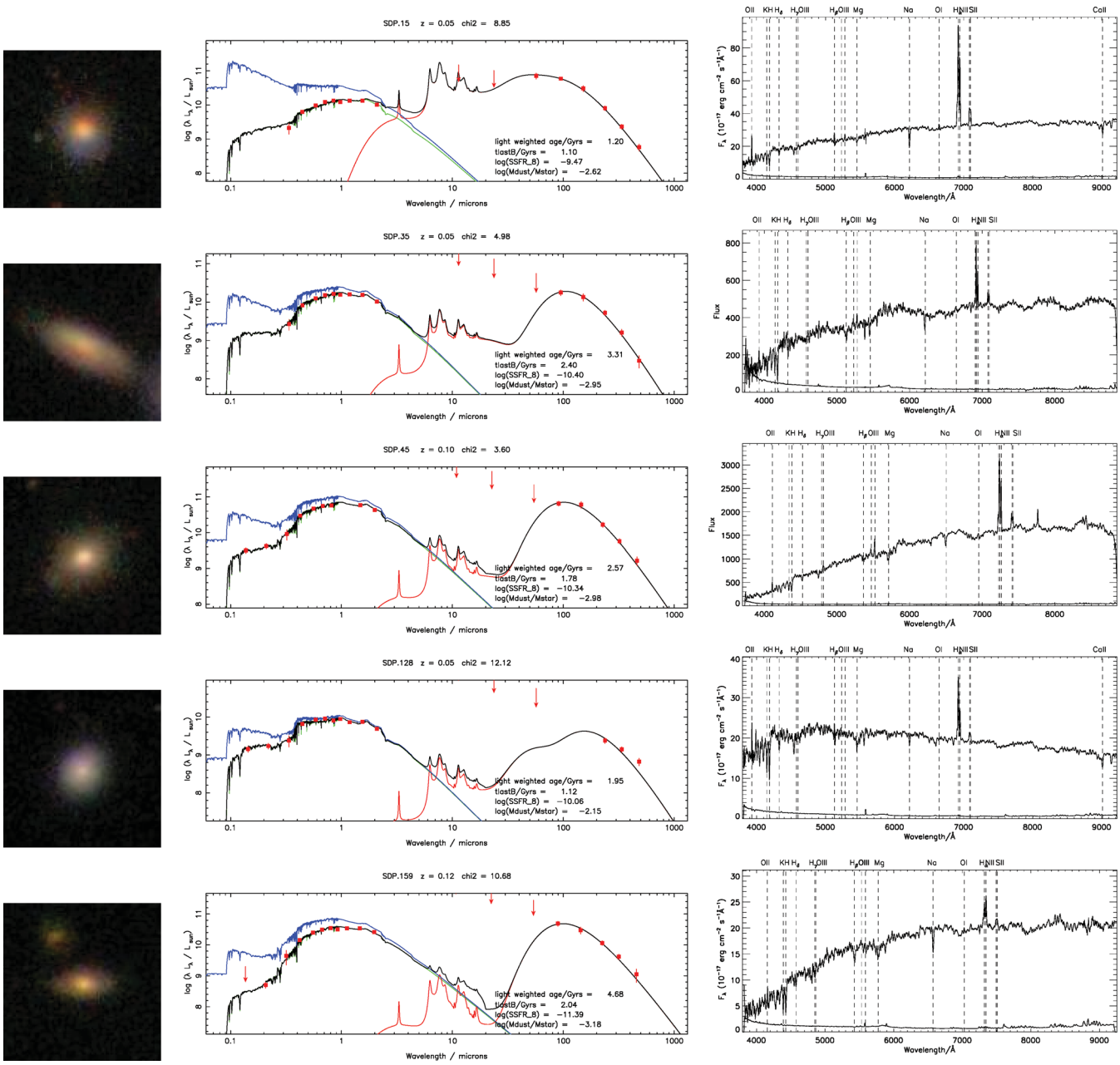

Figure A1. Optical images, multiwavelength SEDs and optical spectra of the 42 ETGs in our sample. Images are 30 arcsec on a side. The rest-frame SEDs of each ETG are shown, where red points are the observed photometry, with 5σ upper limits shown as arrows. Errors on the photometry are described in Smith et al. (2011b). The black line is the total best-fitting model; the green line is the attenuated optical model; the blue line is the unattenuated optical model and the red line is the infrared model. Spectra are from SDSS and GAMA, and the standard deviation in the spectra is also shown. The spectra have been smoothed by a boxcar of 8 pixels.

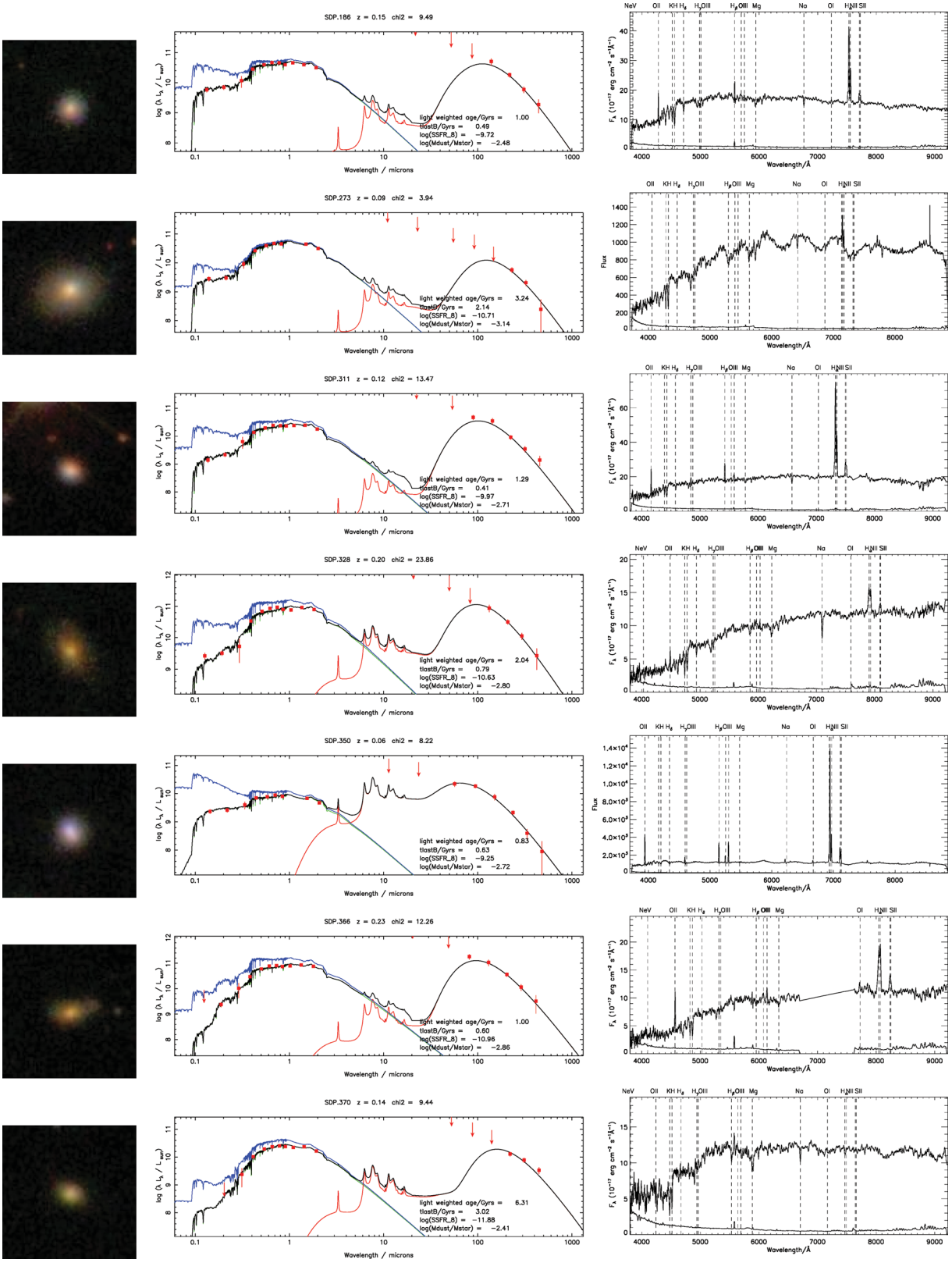

Figure A1 – *continued*

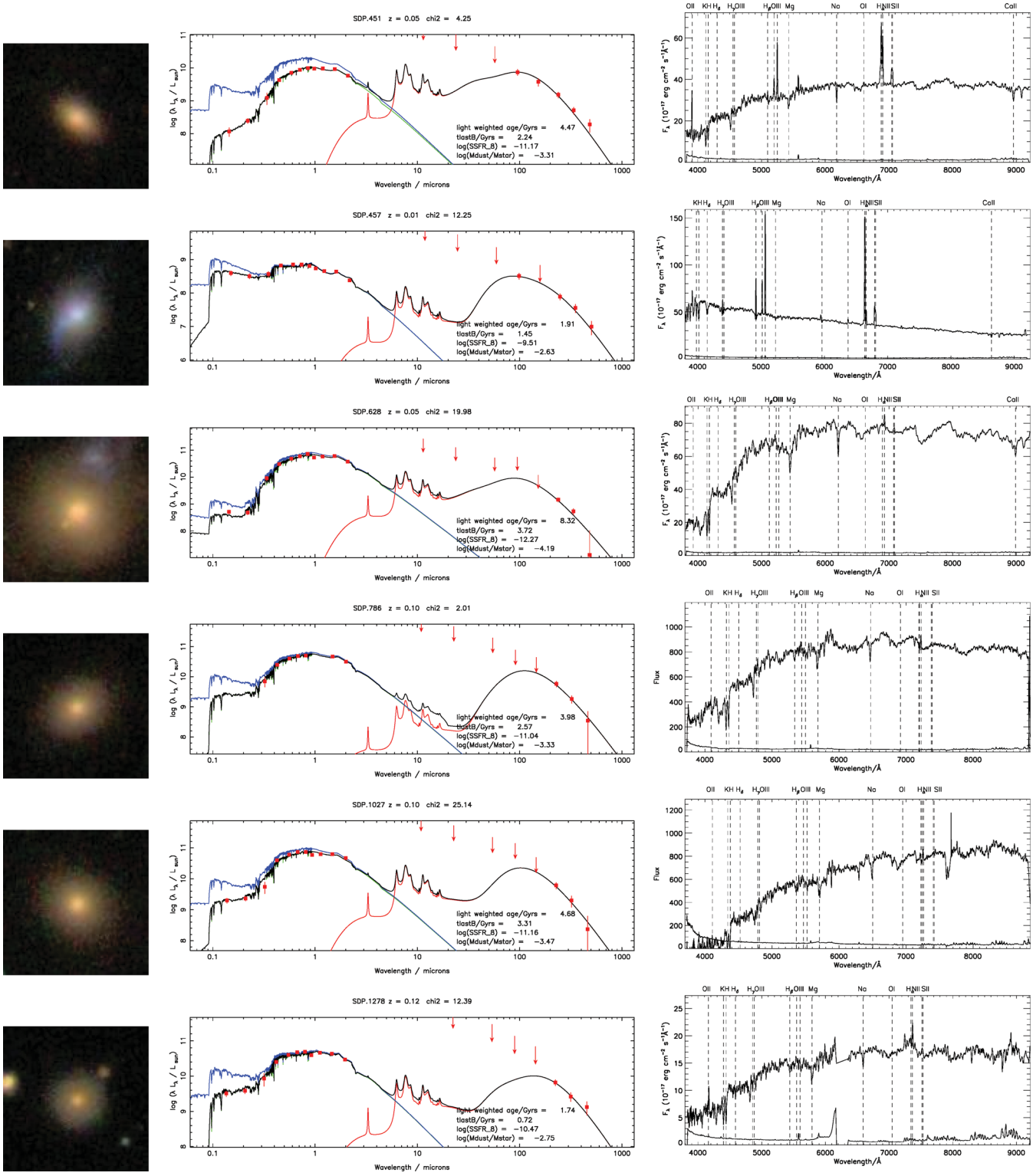

Figure A1 – *continued*

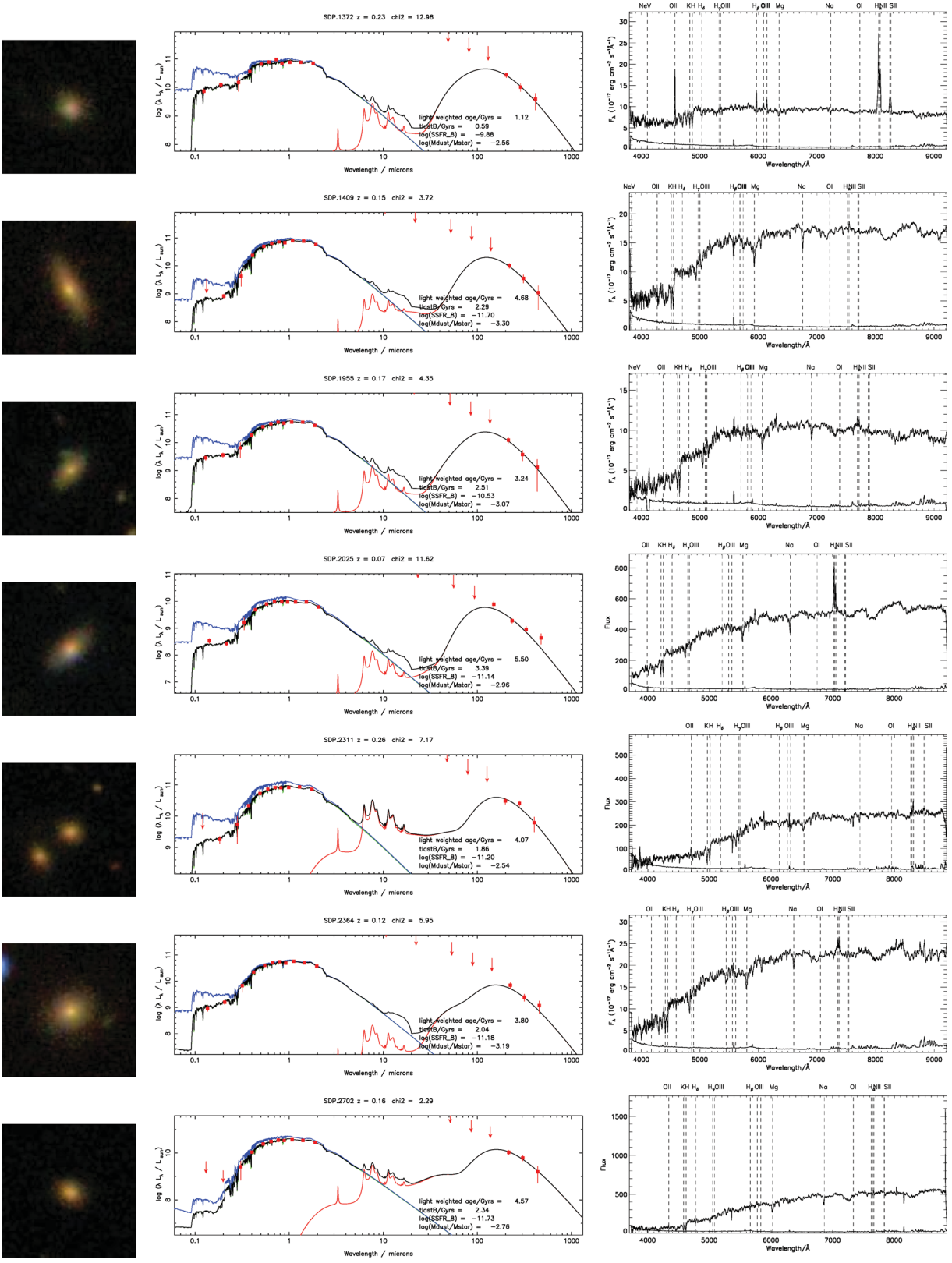

Figure A1 – *continued*

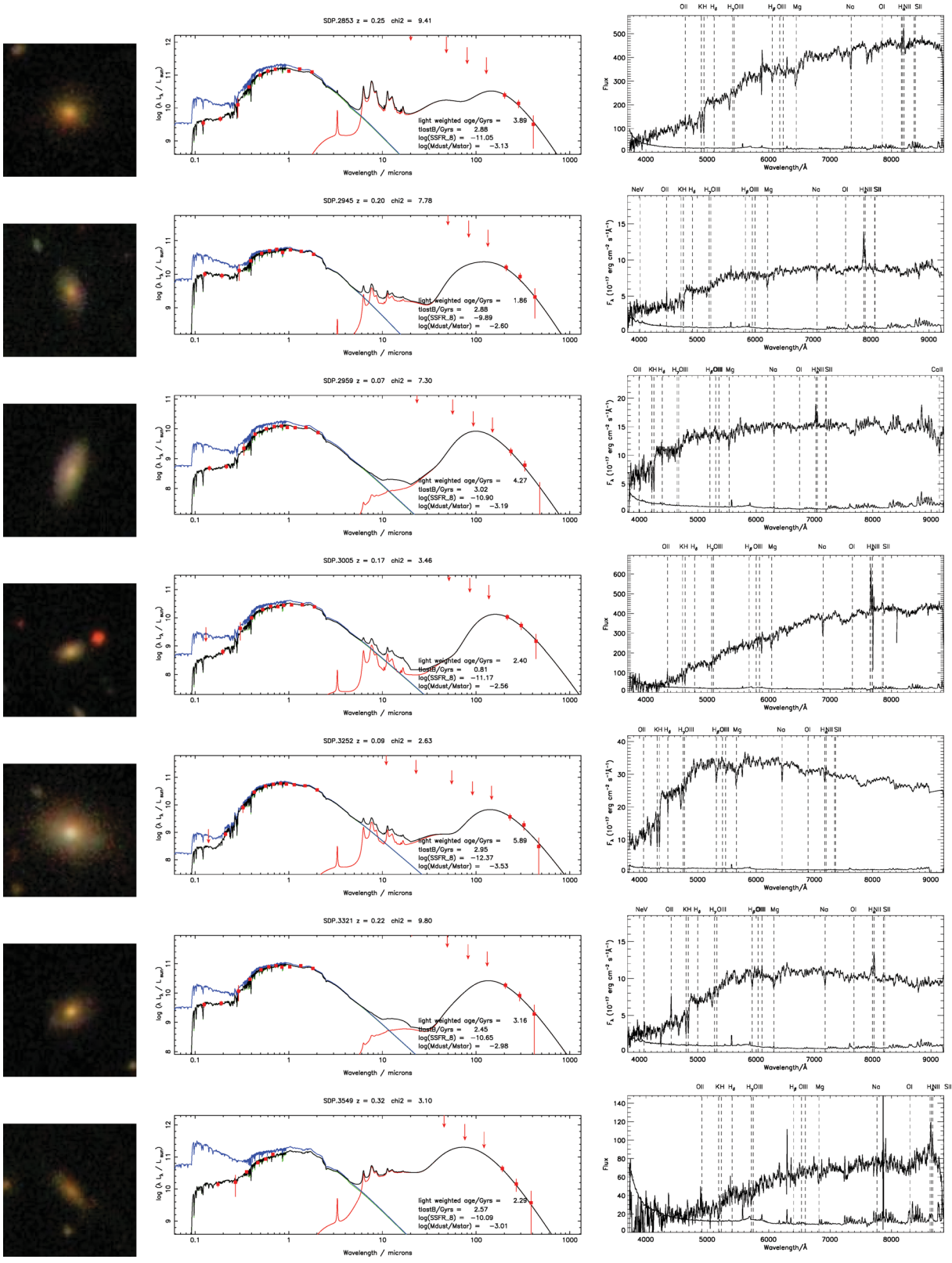

Figure A1 – *continued*

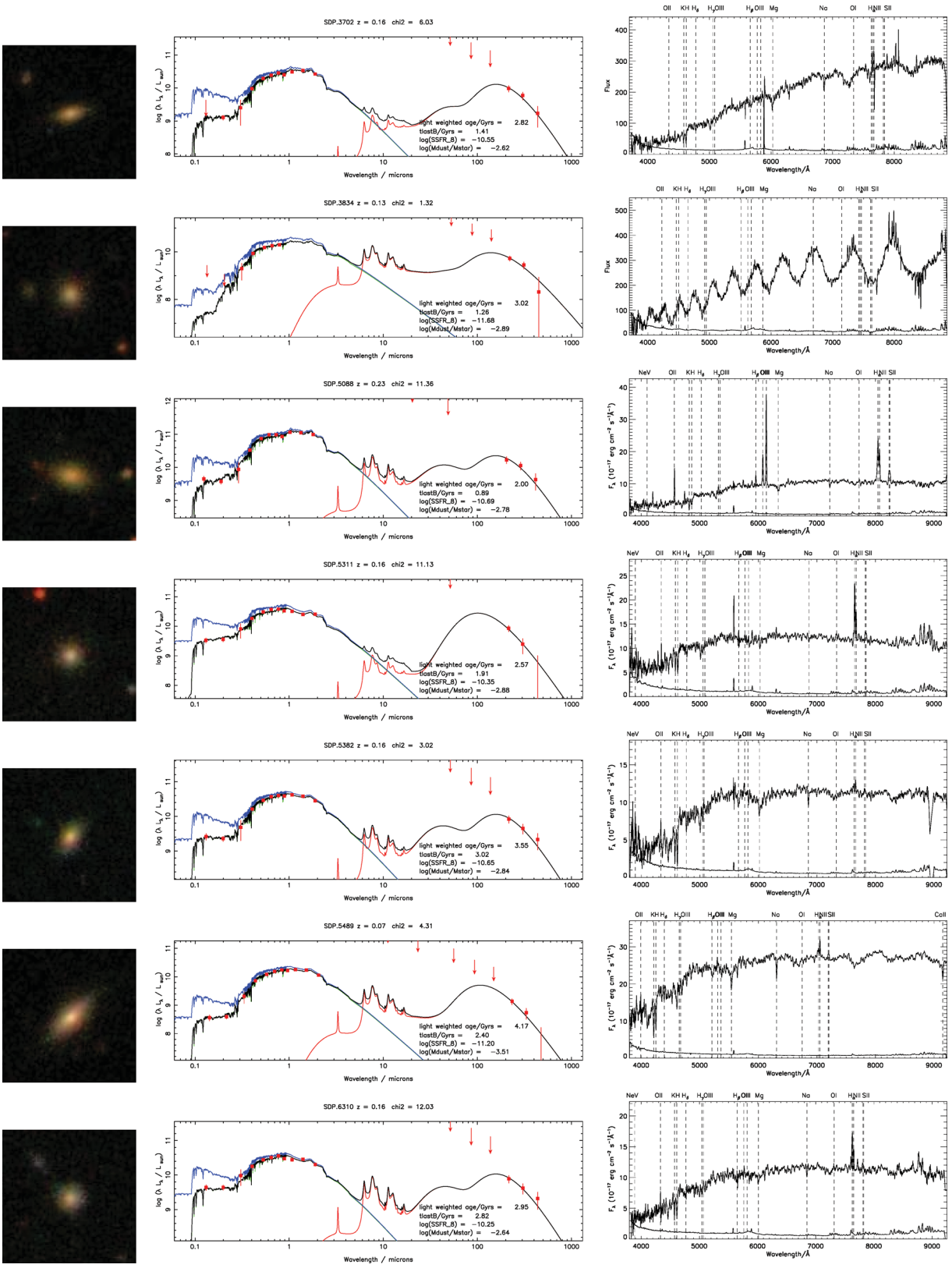

Figure A1 – *continued*. The wave-like features in the spectrum of SDP.3834 are due to fibre fringing (Colless et al. 2001).

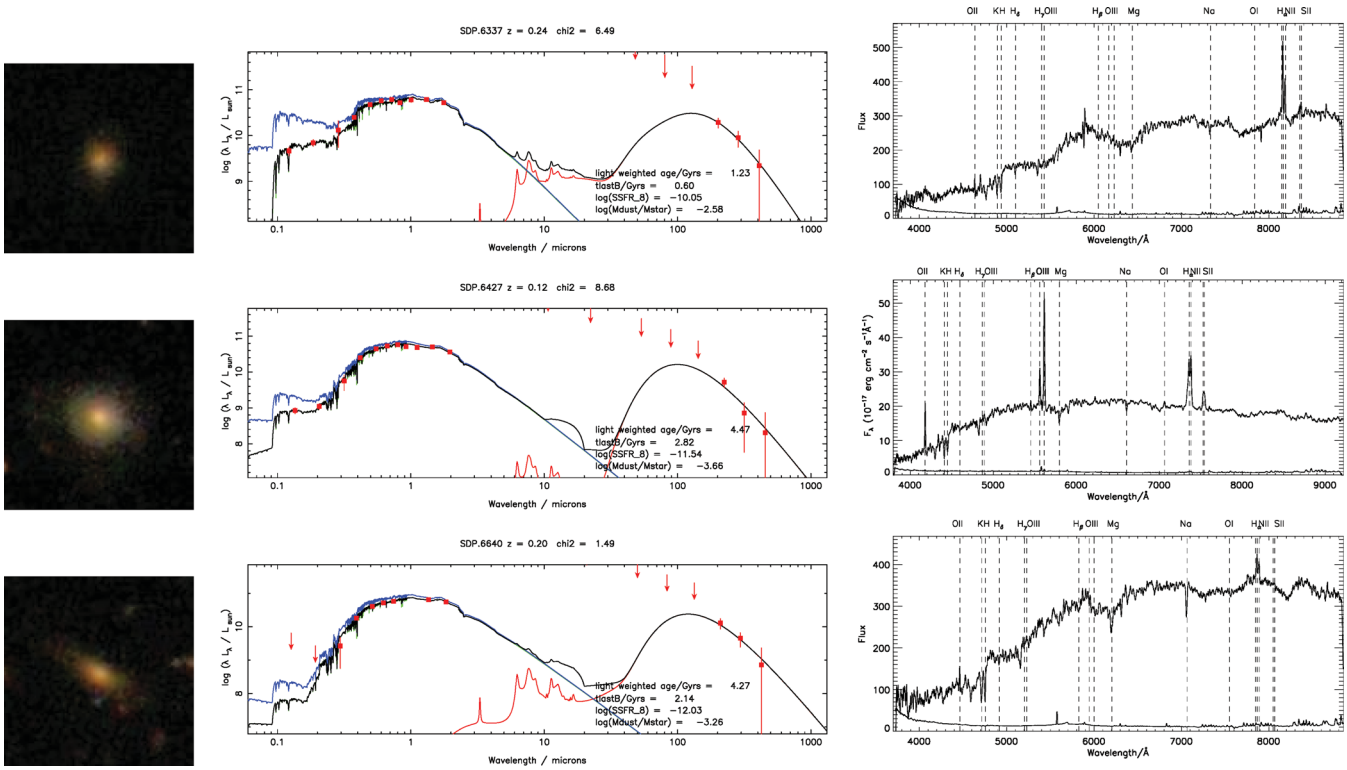

Figure A1 – *continued*

APPENDIX B: PASSIVE SPIRALS

Table B1. Properties of passive spirals derived from SED fitting. The columns are (from left to right): ID, SDP ID, redshift, SDSS RA, SDSS Dec., 250 μm flux in Jy, f_μ, the fraction of total dust luminosity contributed by the diffuse ISM; $\hat{\tau}_V$, total effective V-band optical depth seen by stars in birth clouds; $M_*/M_\odot$, log(stellar mass); $L_d^{tot}/L_\odot$, log(dust luminosity); T_C^{ISM}/K, temperature of the cold ISM dust component; $\hat{\tau}_V^{ISM}$, the V-band optical depth in the ambient ISM. $M_d/M_\odot$, log(dust mass); ψ_S/yr^{-1}, log(SSFR); $\psi/M_\odot yr^{-1}$, log(SFR), t_{LB}, log(time of last burst); age$_r$, log(r-band light-weighted age of the stellar population), rest-frame $NUV - r$ colour (Section 3.4), density (Σ/galaxies Mpc^{-2}, see Section 6) Hα EW/Å (corrected for stellar absorption of 1.3 Å if $>3\sigma$ detection).

ID	SDP ID	z	RA	Dec.	F_{250}	f_μ	$\hat{\tau}_V$	M_*	L_d^{tot}	T_C^{ISM}	$\hat{\tau}_V^{ISM}$	M_d	ψ_S	ψ	t_{LB}	age$_r$	$NUV - r$	Σ	Hα EW
J085828.5+003814	30	0.05	134.619	0.637	0.28	0.87	4.22	10.84	10.39	21.7	0.45	7.50	−11.17	−0.30	9.57	9.77	4.73	0.39	14.77
J090038.0+012810	77	0.05	135.158	1.470	0.19	0.79	1.44	10.86	10.04	17.5	0.17	7.64	−11.14	−0.31	9.39	9.83	4.33	0.19	1.00
J085946.7−000020	143	0.05	134.945	−0.006	0.15	0.85	1.80	10.78	10.15	19.5	0.26	7.45	−11.22	−0.48	9.41	9.65	4.69	0.39	0.57
J090911.8+000029	271	0.08	137.299	0.008	0.12	0.90	2.04	10.53	10.16	18.3	0.52	7.66	−11.25	−0.72	9.18	9.53	5.11	0.18	2.45
J090648.9−005059	372	0.16	136.704	−0.850	0.09	0.94	2.05	11.02	10.73	19.9	0.56	8.05	−11.63	−0.56	9.08	9.45	5.45	0.08	6.06
J090312.4−004509	1544	0.05	135.803	−0.753	0.09	0.67	1.62	10.69	9.88	18.5	0.13	7.23	−11.11	−0.40	9.56	9.73	4.30	–	0.62
J090944.5+022100	1773	0.05	137.435	2.350	0.06	0.94	1.57	10.50	9.78	22.7	0.25	6.76	−12.10	−1.57	8.93	9.62	4.70	0.56	1.63
J090622.3+010014	1888	0.07	136.593	1.004	0.06	0.85	1.13	10.50	9.87	19.8	0.19	7.15	−11.29	−0.76	9.42	9.73	–	0.08	1.01
J085827.1+010426	2547	0.07	134.613	1.074	0.05	0.95	1.66	10.34	9.61	19.8	0.27	6.98	−12.19	−1.91	9.44	9.71	5.29	6.78	2.01
J090543.6+010754	2612	0.05	136.432	1.132	0.05	0.92	2.00	9.94	9.45	20.3	0.40	6.74	−11.53	−1.56	9.19	9.56	5.08	0.22	4.25
J090547.8+001136	3578	0.16	136.450	0.193	0.04	0.92	2.24	10.95	10.48	20.0	0.56	7.78	−11.55	−0.58	9.36	9.63	>4.57	0.14	1.64
J091311.5+001619	3935	0.17	138.299	0.274	0.04	0.94	2.44	10.71	10.27	18.9	0.46	7.72	−11.72	−1.07	9.36	9.69	>4.73	0.28	69.03
J085738.2+010740	4548	0.07	134.410	1.128	0.04	0.91	1.72	10.36	9.72	20.6	0.28	6.96	−11.56	−1.21	9.20	9.58	4.97	4.37	4.65
J090646.2−004453	4639	0.16	136.693	−0.749	0.04	0.85	1.51	10.99	10.48	21.2	0.30	7.57	−11.21	−0.17	9.48	9.73	–	0.17	–
J091144.5+012952	4859	0.17	137.936	1.499	0.04	0.88	2.57	10.85	10.59	21.4	0.79	7.70	−11.04	−0.21	9.32	9.59	>4.29	2.22	2.05
J090013.7+004139	4964	0.24	135.057	0.693	0.04	0.94	2.33	10.49	10.48	17.6	0.48	8.15	−11.41	−0.93	8.70	9.05	4.26	–	9.60
J090707.3+000805	5108	0.10	136.78	0.135	0.04	0.88	2.00	10.21	9.88	18.1	0.47	7.41	−11.13	−0.90	9.13	9.52	4.59	0.09	17.53
J091230.6−005442	5226	0.16	138.128	−0.913	0.04	0.91	2.07	10.75	10.40	19.3	0.44	7.79	−11.26	−0.50	9.10	9.49	4.85	3.12	1.30
J085934.4−000456	7324	0.17	134.895	−0.082	0.03	0.92	1.97	10.73	10.28	19.6	0.43	7.65	−11.50	−0.75	9.24	9.56	>4.72	2.12	2.55

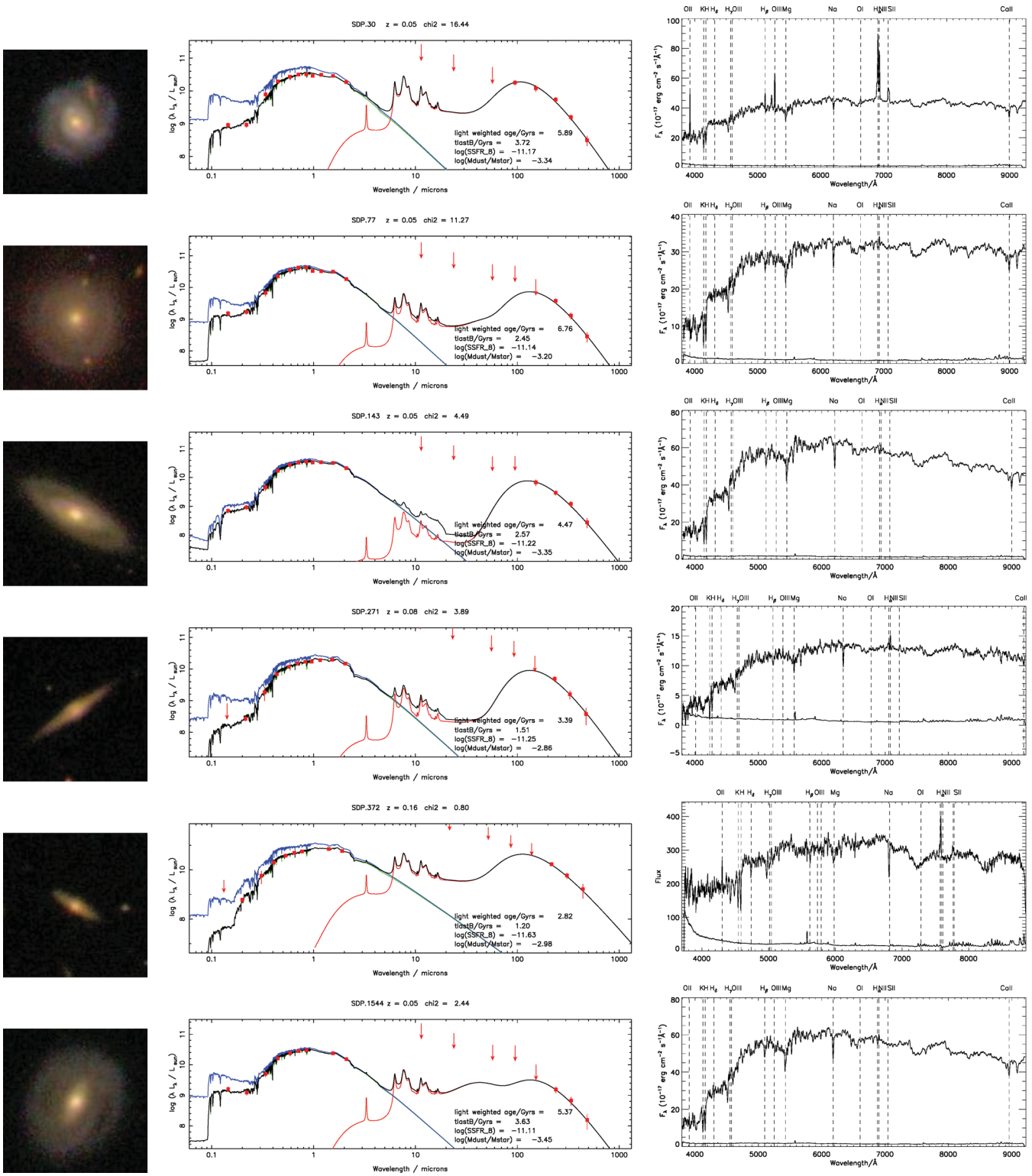

Figure B1. Optical images, multiwavelength SEDs and optical spectra of the 19 passive spirals in our sample. Images are 40 arcsec on a side. The rest-frame SEDs of each passive spiral are shown, where red points are the observed photometry, with 5σ upper limits shown as arrows. Errors on the photometry are described in Smith et al. (2011b). The black line is the total best-fitting SED model; the green line is the attenuated optical model; the blue line is the unattenuated optical model and the red line is the infrared model. Spectra are from SDSS and GAMA, and the standard deviation in the spectra is also shown. The spectra have been smoothed by a boxcar of 8 pixels.

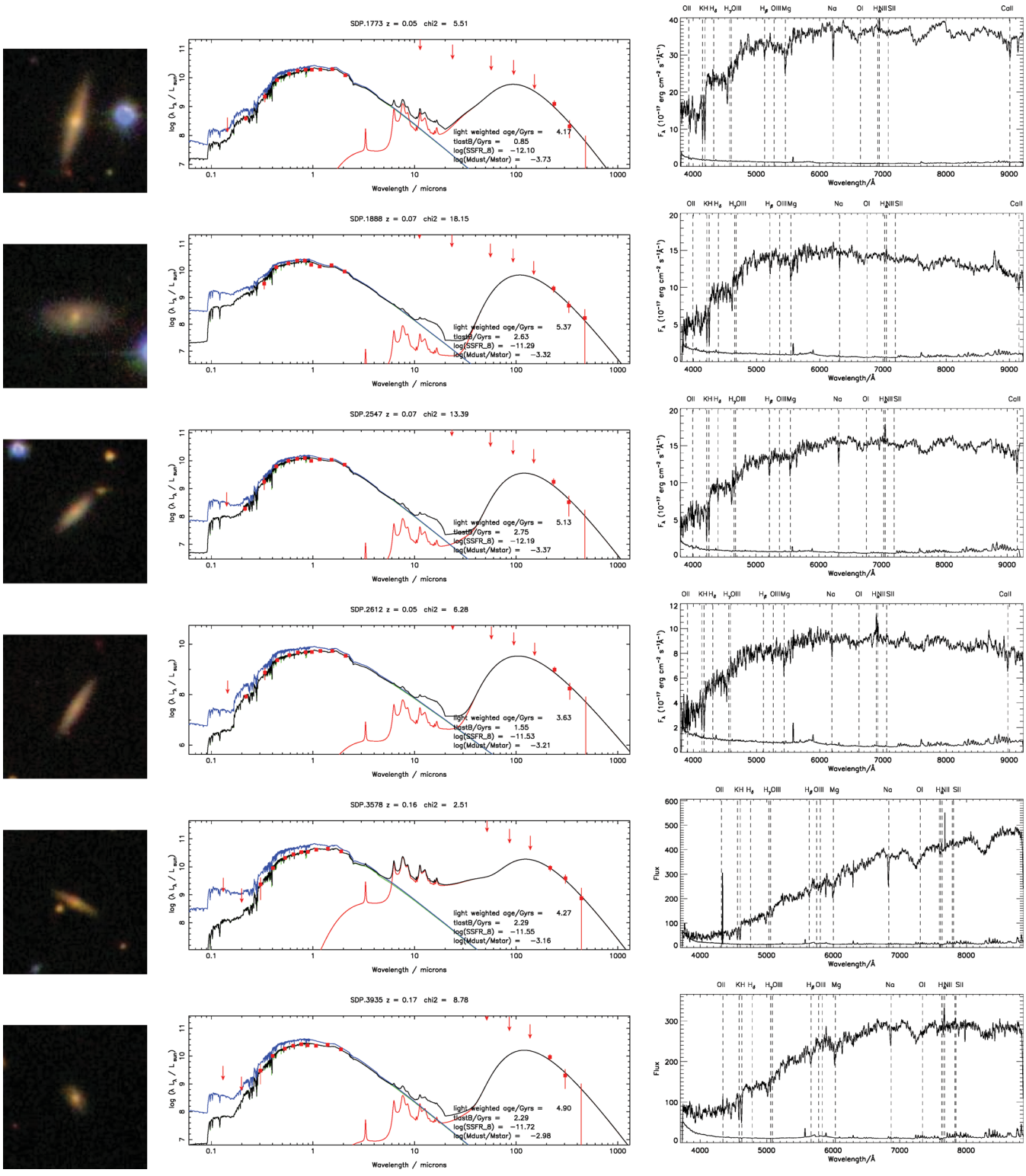

Figure B1 – *continued*

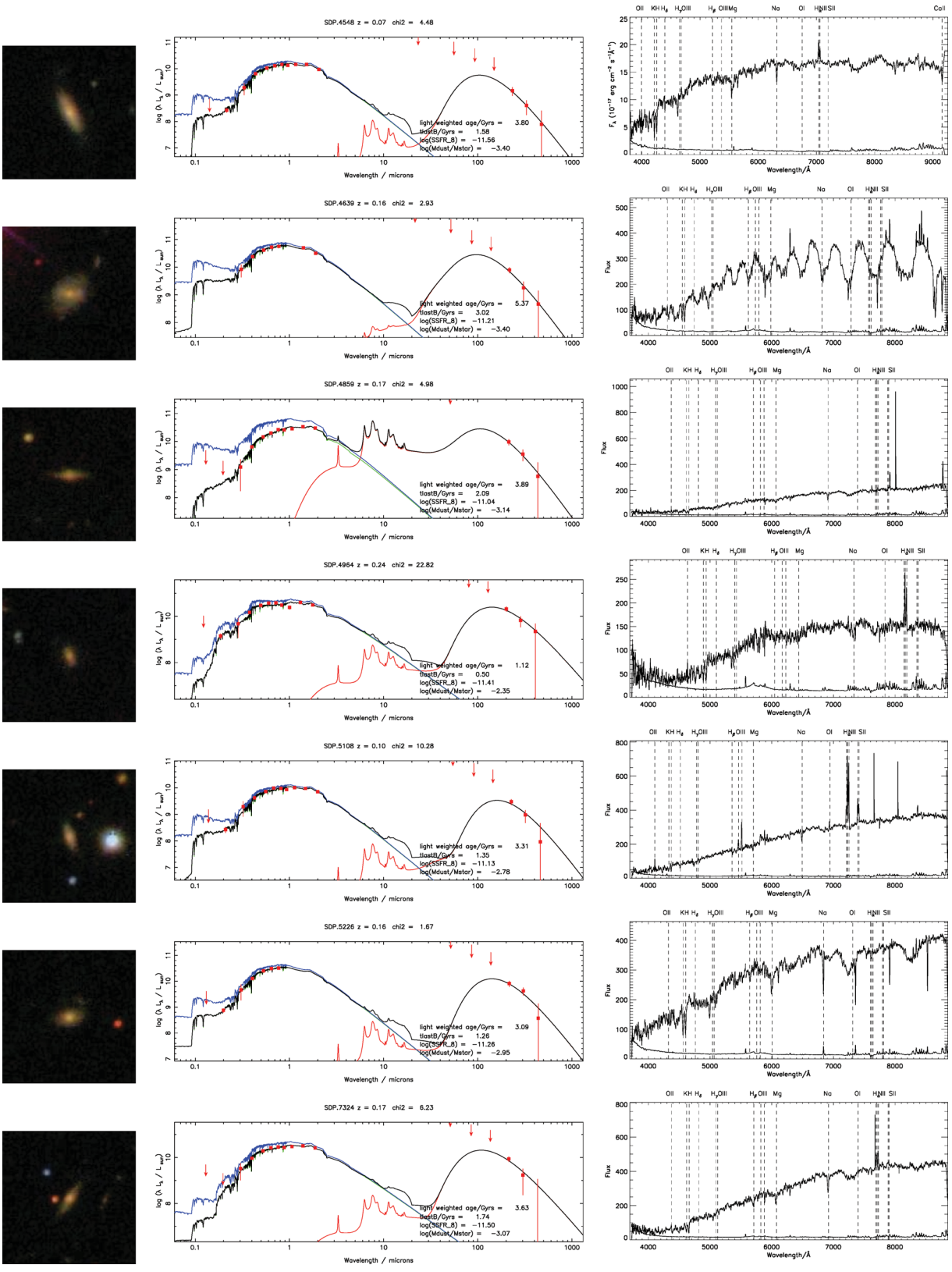

Figure B1 – *continued*. The wave-like features in the spectrum of SDP.4639 are due to fibre fringing (Colless et al. 2001).

APPENDIX C: SUMMARY OF MEAN PHYSICAL PROPERTIES

Table C1. Summary of mean physical properties derived from stacking of PDFs for the different populations studied in this paper. The parameters are: f_μ, the fraction of total dust luminosity contributed by the diffuse ISM; $M_*/\mathrm{M}_\odot$, log(stellar mass); $M_\mathrm{d}/\mathrm{M}_\odot$, log(dust mass); M_d/M_*, log(dust-to-stellar mass ratio); $L_\mathrm{d}^\mathrm{tot}/\mathrm{L}_\odot$, log(dust luminosity); $T_\mathrm{C}^\mathrm{ISM}/\mathrm{K}$, temperature of the cold ISM dust component; $\hat{\tau}_V$, total effective V-band optical depth seen by stars in birth clouds; $\hat{\tau}_V^\mathrm{ISM}$, the V-band optical depth in the ambient ISM, $\psi_\mathrm{S}/\mathrm{yr}^{-1}$, log(SSFR); $\psi/\mathrm{M}_\odot\ \mathrm{yr}^{-1}$, log(SFR), t_LB, log(time of last burst); age_r, log(r-band light-weighted age of the stellar population). For each parameter, we use the first moment of the average PDF to estimate the mean for the population. We can estimate the variance on the population mean as the second moment of the average PDF minus the mean squared, divided by the number of galaxies in the sample. The error on the mean is simply the square root of the population variance. The errors for logarithmic parameters are in dex. The mean parameters from the infrared part of the SED and energy balance parameters are not determined for the control sample, since we only have constraints from upper limits on the FIR-submillimetre flux.

Parameter	H-ATLAS spiral	H-ATLAS ETG	Normal spiral	Passive spiral	Control spiral	Control ETG
f_μ	0.59 ± 0.01	0.74 ± 0.02	0.58 ± 0.01	0.87 ± 0.02	–	–
M_*	10.29 ± 0.02	10.69 ± 0.08	10.27 ± 0.02	10.62 ± 0.07	10.15 ± 0.03	10.77 ± 0.03
M_d	7.72 ± 0.02	7.74 ± 0.08	7.73 ± 0.02	7.47 ± 0.10	–	–
M_d/M_*	-2.57 ± 0.02	-2.95 ± 0.07	-2.54 ± 0.02	-3.16 ± 0.09	–	–
$L_\mathrm{d}^\mathrm{tot}$	10.53 ± 0.02	10.48 ± 0.07	10.55 ± 0.02	10.14 ± 0.09	–	–
$T_\mathrm{C}^\mathrm{ISM}$	19.7 ± 0.1	19.8 ± 0.5	19.7 ± 0.1	19.8 ± 0.6	–	–
$\hat{\tau}_V$	2.28 ± 0.07	2.28 ± 0.23	2.28 ± 0.07	2.34 ± 0.37	1.66 ± 0.08	1.61 ± 0.10
$\hat{\tau}_V^\mathrm{ISM}$	0.47 ± 0.01	0.43 ± 0.04	0.48 ± 0.02	0.41 ± 0.05	0.24 ± 0.01	0.20 ± 0.01
ψ_S	-9.99 ± 0.03	-10.85 ± 0.14	-9.92 ± 0.03	-11.59 ± 0.18	-10.58 ± 0.07	-11.92 ± 0.07
ψ	0.30 ± 0.03	-0.16 ± 0.12	0.36 ± 0.03	-0.97 ± 0.19	-0.43 ± 0.05	-1.16 ± 0.07
t_LB	8.70 ± 0.07	9.04 ± 0.18	8.68 ± 0.08	9.26 ± 0.10	8.87 ± 0.07	9.39 ± 0.03
age_r	9.21 ± 0.02	9.45 ± 0.05	9.19 ± 0.02	9.59 ± 0.05	9.32 ± 0.02	9.67 ± 0.01

This paper has been typeset from a TEX/LATEX file prepared by the author.